
DEVELOPING DISTANCE-AWARE, AND EVIDENT UNCERTAINTY QUANTIFICATION IN DYNAMIC PHYSICS-CONSTRAINED NEURAL NETWORKS FOR ROBUST BEARING DEGRADATION ESTIMATION

Waleed Razzaq

School of Automation

University of Science and Technology China
Hefei, Anhui
waleed.razzaq@mail.ustc.edu.cn

Yun-Bo Zhao *

School of Automation

University of Science and Technology China
Hefei, Anhui
ybzhao@ustc.edu.cn

December 19, 2025

ABSTRACT

Accurate and uncertainty-aware degradation estimation is critical for predictive maintenance in safety-critical systems. Despite advances in uncertainty quantification methods, most existing approaches lack confidence calibration, are computationally expensive, are not distance-aware, and struggle to generalize under out-of-distribution (OOD) data. In this paper, we developed two methods for distance-aware uncertainty quantification in deterministic Physics-constrained neural networks (UQ-PCNNs): (1) PC-SNGP, based on Spectral Normalization Gaussian Process (SNGP), and (2) PC-SNER, based on Deep Evidential Regression (DER). First, we apply spectral normalization to the hidden layer weights of the PCNN to ensure distance-preserving transformations from input space to latent space. In PC-SNGP, the standard dense output layer is replaced with a Gaussian Process layer, enabling distance-sensitive uncertainty estimation. In PC-SNER, we modify the output dense layer to produce the parameters of the Normal Inverse Gamma (NIG) distribution, allowing it to estimate distance-aware uncertainty within a coherent probabilistic framework. To evaluate the effectiveness of both methods, we employ several well-established performance metrics to comprehensively assess the predictive accuracy. Additionally, we introduce a distance-aware performance metric based on Pearson Correlation Coefficient (PCC), which quantifies how sensitively the predicted uncertainty reflects the distance between test samples and the training data. We also develop a dynamic weighting mechanism in the PCNN loss function, enabling the model to adaptively balance data fidelity and physical consistency during training. We conduct a case study to estimate REBs degradation using the PRONOSTIA, XJTU-SY, and HUST datasets, comparing their performance with Monte Carlo-based PCNN (PC-MC) and Deep-Ensemble-based PCNN (PC-DE) using standard and custom metrics. Results show that our methods substantially improve prediction accuracy with minimal variance in out-of-distribution and cross-validation samples. Both PC-SNGP and PC-SNER also demonstrate strong robustness to adversarial attacks and noise.

Keywords Uncertainty Quantification · Physics-constrained neural networks · Epistemic and Aleatoric Uncertainty · PRONOSTIA

1 Introduction

Uncertainty quantification (UQ) involves assessing the degree of confidence in a system's predictions and is commonly categorized into two types: *aleatoric uncertainty*, arising from inherent variability or noise in data; and *epistemic uncertainty*, stemming from incomplete knowledge or uncertainty in model parameters [1]. UQ is critical in high-stakes applications where decision-making errors can lead to significant economic consequences. One of the prominent

*Corresponding author. Email: ybzhao@ustc.edu.cn

challenges in the industrial landscape is accurately estimating the degradation of rolling-element bearings (REBs), which account for about 40% to 50% of failures in industrial rotating machinery [2]. These failures are often attributed to operating under harsh temperatures and variable load conditions. To solve this problem, substantial research has focused on predictive modeling strategies, which are typically divided into two broad categories: (1) physics-based models (PBMs) and (2) data-driven models (DDMs).

PBMs utilize differential equations derived from first principles to represent system degradation. These models are component-specific and adhere to physical laws, ensuring consistency and interpretability. Guo et al. [3] introduced a quasi-static degradation model for REBs that integrates centrifugal expansion, thermal deformation, load distribution, and Hertzian contact mechanisms to enhance stress distribution estimation. Gabrieli et al. [4] introduced a degradation assessment approach based on the Equivalent Damaged Volume (EDV) concept, which combines run-to-failure experimental data with a lumped parameter model. The EDV quantifies defect severity by comparing measured vibration signals to those generated through simulation based on defect geometry. Yang et al. [5] developed an electromechanically coupled digital twin incorporating a stepper motor and deep groove ball-bearing dynamics. Their model simulates rolling-element trajectories, contact forces, and vibration signatures under varying speeds and fault conditions. Ohana et al. [6] presented a spall-focused framework incorporating dynamic response modeling, strain field analysis, spall damage progression, and oil debris monitoring for enhanced fault characterization. Despite these advances, PBMs exhibit notable limitations: (1) they require extensive domain expertise and mathematical modeling knowledge; (2) their performance often degrades in complex systems due to unavoidable modeling simplifications; (3) they lack adaptability to real-time operational variations and generally do not support online parameter updating; (4) their robustness to perturbations is limited unless explicitly modeled within mathematical equations; and (5) they do not quantify the uncertainty in their predictions.

DDMs uncover the hidden relationships within condition monitoring data through machine learning (ML) techniques. With the advancement of ML techniques such as CNN [7], LSTM [8], GRU [9], and attention [10], we have seen significant improvement and accomplishment in degradation estimation for REBs. However, most existing approaches have traditionally focused on deterministic, point-based predictions, neglecting the inherent uncertainty in outputs. Liu et al. [8] utilized LSTM to forecast future bearing operation trends with an exponential degradation model used to estimate the RUL. A dynamic 3σ interval combined with a voting mechanism enables adaptive fault-start time prediction. Jiang et al. [11] proposed a hybrid TCN-MSA model that combines a causally inflated temporal CNN to capture long-term dependencies and frequency domain features. A multihead self-attention mechanism was applied to identify feature significance during bearing degradation. Qi et al. [12] extracted advanced entropy and sparsity-based health indicators from multiband filtered signals and selected the optimal indicator via a proposed evaluation criterion. A constrained Support Vector Data Description (SVDD) was used to detect anomalies and identify the Start Prediction Time (SPT).

Recently, increasing attention has turned to quantifying uncertainty in DDMs, recognizing their importance in safety-critical applications. Contemporary research can be categorized into two types based on methodological approach used: (1) deterministic models and (2) probabilistic models. Deterministic modeling uses the same deterministic feed-forward neural network (NN) and models the output layer to predict the mean μ and variance σ^2 [13]. Pan et al. [14] proposed a meta-weighted NN with three subnetworks—drift, diffusion, and weight nets—for predicting the RUL of turbopump bearings. Their approach integrates meta-learning-based sample reweighting to mitigate negative transfer and diffusion-based uncertainty estimation to distinguish between in-and out-of-distribution data. The method utilizes convolutional architectures and fine-tuned gradient-based optimization to adaptively improve the prediction accuracy and reliability across domains. Probabilistic models extend traditional deterministic approaches by predicting distributions over outcomes or model parameters [15]. Jiang et al. [16] proposed a CNN-LSTM-based model enhanced with Bayesian neural networks (BNN) to predict the RUL of REBs. Their method integrates convolutional feature extraction, temporal pattern learning via LSTM, and UQ through variational inference in the BayesLSTM framework. Rivas et al. [17] proposed a BNN using the Bayes by Backprop algorithm and variational inference to predict the RUL and uncertainty for turbofan engines. Their methodology includes time window-based feature construction, two-step filtering (Savitzky-Golay and exponential), and z-score normalization of sensor data. Song et al. [18] introduced a model based on Fractional Brownian Motion (FBM) to capture the long-range dependence and self-similarity in bearing degradation signals. Their methodology comprises three stages: feature decomposition using Variational Mode Decompositions (VMD), metric-based component selection for health indicator (HI) construction, and FBM-driven degradation modeling with parameters estimated via maximum likelihood estimation and RL inferred using Monte Carlo simulations. Ochella et al. [19] proposed a deep BNN utilizing MC dropout to estimate RUL by directly modeling both aleatoric and epistemic uncertainties. The features are selected based on trendability, prognosability, and monotonicity metrics. Despite significant progress in DDMs approaches, several limitations persist: (1) they require large volumes of high-quality labeled degradation data for effective estimation; (2) their computational complexity increases significantly with model depth and the number of nonlinear parameters, complicating deployment on resource-constrained platforms;

(3) these models often operate as black boxes, lacking interpretability, explainability, and adherence to physical laws; and (4) quantified uncertainty is not distance-aware, failing to account for distribution shifts between training and test data.

To address the limitations inherent in both PBM_s and DDM_s, a hybrid paradigm has emerged, commonly referred to Physics-constrained Neural Networks (PCNN_s). PCNN_s aim to integrate the rigor and interpretability of PBM_s with the flexibility and pattern recognition capabilities of DDM_s, thereby enhancing prediction accuracy, robustness, and model transparency. Compared with PBM_s, PCNN_s reduce the dependence on expert-defined differential equations and allow for parameter uncertainty, improving flexibility. Relative to DDM_s, PCNN_s require smaller training datasets and involve fewer nonlinear parameters, facilitating faster convergence and better generalization to unseen data. By embedding known physical constraints into the model architecture or loss function, PCNN_s provide a degree of interpretability, addressing the black-box nature of DDM_s [20].

Similar to DDM_s, most of the work on PCNN_s for the degradation estimation of REBs has centered around deterministic fixed-point modeling. Chao et al. [21] developed a physics-based calibration model for sensor data, which was used to supervise the NN's learning process. Yin et al. [22] utilized phase space reconstruction combined with a compact CNN and monotonic constraints, encoding degradation physics in the input space to enhance learning quality. Zhuo et al. [23] applied a wavelet neural network (WNN) to time-domain features extracted through empirical mode decomposition for robust RUL estimation. Yucsan et al. [24] introduced a custom RNN cell design that incorporates lubrication degradation physics and a reduced-order model into the network structure. Lu et al. [25] proposed a PI-LSTM that uses an adaptive loss function weighting to enforce RUL degradation consistency. Hu et al. [26] designed a hybrid DSCN-AttnPINN that combines a deep separable convolution, an attention mechanism, and a PINN.

Uncertainty quantification in PCNN_s (UQ-PCNN_s) is a relatively emerging field with existing architectures such as Bayesian PCNN_s (PC-BNN_s) [27], Monte Carlo-dropout PCNN_s (PC-MC_s) [28], and deep ensemble PCNN_s (PC-DE_s) [29]. These approaches suffer from high computational costs and require large labeled datasets, which undermines the efficiency benefits of PCNN_s. Additionally, these models are generally not distance-aware, meaning that the estimated uncertainty at observed input points is expected to be near zero, while predictive uncertainty should increase as test inputs move further away from the training data. Distance-aware and confident UQ-PCNN research remains nascent, requiring attention to developing robust, scalable, and interpretable solutions.

To build upon this, we propose two principled distance-aware UQ-PCNN methods: (1) PC-SNGP, based on Spectral Normalization Gaussian Process (SNGP) [30]; and (2) PC-SNER, based on Deep Evidential Regression (DER) [31]. Both are integrated into a single deterministic end-to-end NN. In both variants, spectral normalization [32] is applied to all layers except the outputs to preserve distance-aware hidden mapping. In PC-SNGP, the output layer is replaced by a Gaussian process with a radial basis function (RBF) kernel, providing distance-sensitive uncertainty estimates. The PC-SNER variant modifies the dense output layer to produce parameters of a Normal-Inverse Gamma (NIG) distribution [33], enabling joint approximation of the distance-aware predictive mean and variance. Furthermore, a dynamic loss weighting strategy is implemented into the Physics-constrained loss (PC-loss) to maintain alignment between the estimated degradation and a physics-based degradation model, which includes fatigue, wear, and lubrication degradation components. The key contributions of this research are as follows:

1. We developed two distance-aware deterministic UQ-PCNN variants, PC-SNGP and PC-SNER, that provide distance-aware and evidential uncertainty quantification.
2. A comprehensive physics-based degradation model incorporating fatigue, wear, lubrication, temperature dynamics with interlinked feedback and stochastic contamination is proposed to enhance the physical relevance of the predictions.
3. A dynamic weighting strategy is introduced in Physics-constrained loss to make it adaptive and ensure consistency between predictions and physical degradation trends.
4. The effectiveness is validated through experiments on the PRONOSTIA dataset, while cross-validation is performed on the XJTU-SY and HUST benchmark datasets.

The remainder of this paper is organized as follows: Section 2 presents the theoretical foundations of both methods, including an overview of the PCNN_s, SNGP, and DER. Section 3 provides a detailed case study using the PRONOSTIA dataset, covering the problem formulation, dataset description, data curation, evaluation metrics, training procedures, and computational results. Section 4 discusses the broader implications and potential impact, and future aspects of the research. Finally, Section 5 concludes the paper.

2 Theoretical Foundations of Methods

2.1 Problem Setup

Consider a data-generating distribution $p^*(y | x)$, where $y \in \mathbb{R}$ denotes the estimated degradation, and $x \in \mathcal{X} \subset \mathbb{R}^D$ represents the input data manifold, equipped with a suitable metric $\|\cdot\|_{\mathcal{X}}$. In practice, the training dataset $\mathcal{D} = \{(x_i, y_i)\}_{i=1}^N$ constitutes a finite sample drawn from a restricted region $\mathcal{X}_{\text{IND}} \subset \mathcal{X}$, commonly referred to as the *in-domain* input space. Consequently, the overall data-generating distribution can be viewed as a mixture comprising an in-domain component $p_{\text{IND}}(y | x) = p^*(y | x, x \in \mathcal{X}_{\text{IND}})$, and an out-of-distribution (OOD) component $p_{\text{OOD}}(y | x) = p^*(y | x, x \notin \mathcal{X}_{\text{IND}})$. During training, the PCNN learns exclusively from \mathcal{D} , the REBs sy acquiring knowledge of the $p_{\text{IND}}(y | x)$, while remaining agnostic to the structure and behavior of $p_{\text{OOD}}(y | x)$. A key requirement is to reliably estimate predictive uncertainty is its capacity to quantify—either explicitly or implicitly—the likelihood that a test input x belongs to the \mathcal{X}_{IND} . This, in turn, requires the model to possess a meaningful notion of *distance* (or *dissimilarity*) between x and \mathcal{X}_{IND} , as measured by the metric $\|\cdot\|_{\mathcal{X}}$ defined over the data manifold.

In the context of degradation estimation of REBs, \mathcal{X}_{OOD} corresponds to operational conditions, sensor readings, or failure modes that are not represented in \mathcal{X}_{IND} . These inputs typically do not have a meaningful correspondence with the in-domain labels $y_{\text{IND}} \in \mathbb{R}$, which are derived from known degradation patterns within \mathcal{X}_{IND} . As a result, $p^*(y | x, x \notin \mathcal{X}_{\text{IND}})$ may differ significantly from $p^*(y | x, x \in \mathcal{X}_{\text{IND}})$, and we can only expect the model to make reliable predictions within \mathcal{X}_{IND} . However, during deployment, the model must produce distance-aware predictive distribution $p(y | x)$ across the entire input space $\mathcal{X} = \mathcal{X}_{\text{IND}} \cup \mathcal{X}_{\text{OOD}}$, since real-world machinery may encounter previously unseen conditions or fault types.

Importance of distance awareness: Distance-awareness means that the estimated uncertainty at observed input points is expected to be near zero, while predictive uncertainty should increase as test inputs move further away from the training data. Distance awareness is essential for high-risk safety-critical tasks because it allows models to identify inputs that deviate from the training manifold, avoiding unreliable predictions under unseen conditions that could lead to machinery failures. By measuring dissimilarity from \mathcal{X}_{IND} , it improves uncertainty estimates and enables safer maintenance decisions through timely alerts for intervention or further data collection.

2.2 Proposed solution

Existing models, such as B-PCNNs, are capable of capturing aleatoric uncertainty but largely remain agnostic to epistemic uncertainty. Deterministic approaches like Monte Carlo (PC-MC), which approximate Bayesian inference, and Deep Ensemble (PC-DE) can characterize epistemic uncertainty; however, they lack distance-awareness in their uncertainty estimates. To overcome this limitation, this paper proposes two variants of deterministic UQ-PCNNs: (1) PC-SNGP, based on Spectral Normalization Gaussian Process, and (2) PC-SNER, based on Spectral Normalization Deep Evidential Regression. In both cases, the key steps include applying spectral normalization to the weight matrices of the hidden layers in PCNNs to preserve Lipschitz continuity during the transformation from input space to latent space; and either replacing the standard dense output layer with a Gaussian Process layer in PC-SNGP, or modifying the output layer to parameterize the Normal-Inverse Gamma distribution in PC-SNER. These modifications enable distance-aware uncertainty estimation, addressing the shortcomings of existing methods.

2.2.1 Dynamic Physics-Constrained Neural Networks (PCNNs)

PCNNs extend standard neural network (NN) architectures by embedding physics directly into the learning process, encouraging convergence toward physically consistent solutions. This is typically achieved by augmenting the loss function with a physics-based term, resulting in a total loss of the form:

$$\mathcal{L}_{\text{total}} = \mathcal{L}_{\text{data}} + \mathcal{L}_{\text{phys}} \quad (1)$$

Here, $\mathcal{L}_{\text{data}}$ quantifies the discrepancy between the model's prediction and ground truth observations, whereas $\mathcal{L}_{\text{phys}}$ penalizes deviation from established physical laws. This formulation helps mitigate the black-box nature of NNs by enforcing physical consistency during training.

In the context of degradation estimation, certain feature indicators, such as those that exhibit monotonic trends over time, provide important cues. For example, an increase in specific feature values is expected to correspond to greater degradation. When such relationships are violated, the model's prediction conflicts with physical expectations. To prevent this, $\mathcal{L}_{\text{phys}}$ is computed using automatic differentiation, comparing the time derivative of the network's output D_{phys} with the output of the physical degradation model. However, degradation is inherently complex and nonlinear, and standard PCNNs often struggle to maintain strict monotonicity in their prediction. To address this, we introduce dynamic weighting to the loss components, allowing the model to adaptively balance data fidelity and physical consistency

during training. The weights are defined such that $w_1 + w_2 = 1$, where w_1 and w_2 are calculated as:

$$w_1 = \frac{e^{\sigma_X}}{e^{\sigma_{\text{phys}}} + e^{\sigma_X}}, \quad w_2 = \frac{e^{\sigma_{\text{phys}}}}{e^{\sigma_{\text{phys}}} + e^{\sigma_X}} \quad (2)$$

where $\sigma_{\text{phys}} = \text{StdDev}(D_{\text{phys}})$ and $\sigma_X = \text{StdDev}(\mathcal{X}_{\text{IND}})$. This formulation ensures that the loss contributions are adaptively scaled based on the variability of each component, promoting more stable and self-balanced optimization. The total loss becomes

$$\mathcal{L}_{\text{total}} = w_1 \mathcal{L}_{\text{data}} + w_2 \mathcal{L}_{\text{phys}}. \quad (3)$$

2.2.2 Spectral Normalization

To make the PCNN distance aware, it is essential to ensure that the hidden mapping h preserves distances; that is, the distance between inputs $\|x - x'\|_X$ is approximately maintained in the hidden representation space $\|h(x) - h(x')\|_H$. For networks with residual connections, this can be achieved by ensuring that each nonlinear residual block $\{g_l\}_{l=1}^{L-1}$ is Lipschitz bound with a constant less than 1 [30]. Let the hidden mapping be defined as

$$h = h_{L-1} \circ \dots \circ h_2 \circ h_1, \quad (4)$$

with each residual block defined as $h_l(x) = x + g_l(x)$. If every g_l is α -Lipschitz for some $0 < \alpha < 1$, i.e.,

$$\|g_l(x) - g_l(x')\|_H \leq \alpha \|x - x'\|_X, \quad \forall x, x' \in \mathcal{X}_{\text{IND}}, \quad (5)$$

then the full mapping h satisfies the bi-Lipschitz condition:

$$(1 - \alpha)^{L-1} \|x - x'\|_X \leq \|h(x) - h(x')\|_H \leq (1 + \alpha)^{L-1} \|x - x'\|_X. \quad (6)$$

The proof for Eqn. 6 is available at [30]. To enforce the Lipschitz constraint, it suffices to control the spectral norm of the linear weights W_l in each block $g_l(x) = W_l x + b_l$, since the Lipschitz constant of a linear transformation is upper bounded by its spectral norm: $\|g_l\|_{\text{Lip}} \leq \|W_l\|_2$. Therefore, we apply spectral normalization at each training step:

$$W_l \leftarrow \begin{cases} \frac{c \cdot W_l}{\hat{\lambda}} & \text{if } \hat{\lambda} > c, \\ W_l & \text{otherwise,} \end{cases} \quad (7)$$

where $\hat{\lambda} = \|W_l\|_2$ is the estimated spectral norm and $c < 1$ is the norm-multiplier hyperparameter [30].

2.2.3 PC-SNGP: Physics-Constrained Spectral Normalization Gaussian Process

To make the PCNN output distance-aware, PC-SNGP replaces the dense output $d : H \rightarrow \mathbb{R}$ using a Gaussian process (GP) with RBF kernel, where the posterior variance depends on the Euclidean distance between test and training hidden representations. Let $\mathcal{D} = \{(x_i, y_i)\}_{i=1}^N$ be the training set, and $h_i = h(x_i) \in \mathbb{R}^{D_{L-1}}$ be the penultimate layer outputs. The GP output vector $\mathbf{g} = [g_1, \dots, g_N]^T$ follows $\mathcal{MVN}(\mathbf{0}, K)$, where $K \in \mathbb{R}^{N \times N}$ with entries $K_{ij} = \exp(-\gamma \|h_i - h_j\|_2^2)$, and γ is a tunable RBF kernel parameter. For scalability, the kernel is approximated using Random Fourier Features (RFF):

$$\Phi_i = \sqrt{\frac{2}{D_L}} \cos(W_L h_i + b_L) \quad (8)$$

where $W_L \in \mathbb{R}^{D_L \times D_{L-1}} \sim \mathcal{N}(0, I)$ and $b_L \in \mathbb{R}^{D_L} \sim \mathcal{U}[0, 2\pi]$. The output becomes:

$$g(h_i) = \Phi_i^T \beta = \sqrt{\frac{2}{D_L}} \cos(W_L h_i + b_L)^T \beta, \quad (9)$$

where $\beta \in \mathbb{R}^{D_L}$ is a trainable weight vector. In a Bayesian linear regression setting, $\beta \sim \mathcal{MVN}(\hat{\beta}, \Sigma)$, where $\hat{\beta}$ is the predictive mean and posterior covariance: $\Sigma = I_{D_L} - \Phi K^{-1} \Phi^T$, providing uncertainty estimates while ensuring distance-awareness and physical coherence [30].

Training Objective: PC-SNGP can be trained end-to-end using a maximum likelihood estimation (MLE) objective. In the context of deterministic regression, it is assumed that each target value y_i is drawn independently and identically distributed (i.i.d.) from a Gaussian distribution parameterized by the model's predictive $\hat{\beta}$ and Σ , denoted collectively as θ . These parameters are learned by maximizing the likelihood of observing the target data, that is, by optimizing $p(y_i | \theta)$. This is achieved by minimizing the negative log-likelihood (NLL), which for a Gaussian output distribution takes the form:

$$\mathcal{L}_{\text{MLE}} = -\log p(y_i | \hat{\beta}, \Sigma) = \underbrace{\frac{1}{2} \left[\log(2\pi \text{diag}(\Sigma)) + \frac{(y_i - \hat{\beta})^2}{\text{diag}(\Sigma)} \right]}_{\theta}, \quad (10)$$

where $\text{diag}(\Sigma)$ denotes the predictive variance obtained from the diagonal entries of the posterior covariance matrix. While this likelihood-based formulation effectively captures aleatoric uncertainty, it remains blind to epistemic uncertainty.

2.2.4 PC-SNER: Physics-Constrained Spectral Normalization Evidential Regression

To enable distance-aware evidential uncertainty quantification in PCNNs, PC-SNER modifies the dense output layer with a probabilistic evidential model based on Deep Evidential Regression (DER). Using the same hidden representation $h_i = h(x_i) \in \mathbb{R}^{D_{L-1}}$, the output layer now maps: $d : h(x) \mapsto (\gamma, \nu, \alpha, \beta)$, which parameterizes a Normal-Inverse-Gamma (NIG) distribution over the mean (μ) and variance (σ^2) of a Gaussian likelihood. The choice of the NIG distribution is motivated by the limitations of Prior Networks [34, 35], which place Dirichlet Priors [36] over discrete classification predictions and require OOD data or fixed prior regularization, whereas NIG enables joint modeling of aleatoric and epistemic uncertainty in continuous regression tasks [31]. The NIG distribution becomes:

$$p(\mu, \sigma^2 \mid \underbrace{\gamma, \nu, \alpha, \beta}_{\theta}) = \frac{\beta^\alpha \sqrt{\nu}}{\Gamma(\alpha) \sqrt{2\pi\sigma^2}} \left(\frac{1}{\sigma^2} \right)^{\alpha+1} \exp \left(-\frac{2\beta + \nu(\gamma - \mu)^2}{2\sigma^2} \right) \quad (11)$$

This induces the marginal distribution:

$$\mu \sim \mathcal{N}(\gamma, \frac{\sigma^2}{\nu}), \quad \sigma^2 \sim \Gamma^{-1}(\alpha, \beta), \quad (12)$$

yielding a Student- t distribution over the predictive output y . The predictive mean is $\mathbb{E}[y] = \gamma$, and the predictive variance is

$$\text{Var}[y] = \underbrace{\frac{\beta}{\alpha-1}}_{\text{aleatoric}} + \underbrace{\frac{\beta}{\nu(\alpha-1)}}_{\text{epistemic}} = \frac{\beta(1+\nu)}{\nu(\alpha-1)} \quad (13)$$

capturing both aleatoric and epistemic uncertainty. The output corresponding to the mean γ uses a linear activation, while the remaining parameters ν, α, β are passed through a *softplus* activation to ensure positivity. Additionally, a small positive shift is applied to α ($\alpha \leftarrow \text{softplus}(z) + 1$) to ensure the condition $\alpha > 1$, which is required for the existence of the first moment of the NIG distribution.

Training Objective: PC-SNER is trained end-to-end using a two-term objective designed to both maximize data fit and penalize unwarranted certainty. The first term of the loss is the negative log marginal likelihood under the Student- t distribution. Given a training set $\mathcal{D} = \{(x_i, y_i)\}_{i=1}^N$, and denoting the network's predicted parameters for the i -th sample as $(\gamma_i, \nu_i, \alpha_i, \beta_i)$, the negative log-evidence is defined as

$$\mathcal{L}_{\text{NLE}} = \frac{1}{2} \log \left(\frac{\pi}{\nu_i} \right) - \alpha_i \log(\Omega_i) + \left(\alpha_i + \frac{1}{2} \right) \log [(y_i - \gamma_i)^2 \nu_i + \Omega_i] + \log \left(\frac{\Gamma(\alpha_i)}{\Gamma(\alpha_i + \frac{1}{2})} \right) \quad (14)$$

where $\Omega_i = 2\beta_i(1 + \nu_i)$. This term encourages the network to produce evidence that is consistent with the data by maximizing the marginal likelihood of each target value under the induced predictive distribution. To prevent the network from generating overconfident predictions on erroneous inputs, a regularization term is introduced that penalizes the amount of evidence in proportion to the prediction error. Drawing from the interpretation of the NIG parameters as virtual observations, the total evidence for the i -th sample is given by $\Phi_i = 2\nu_i + \alpha_i$. The regularization loss (\mathcal{L}_{Reg}) is therefore defined as

$$\mathcal{L}_{\text{Reg}} = |y_i - \gamma_i| \cdot \Phi_i = |y_i - \gamma_i| \cdot (2\nu_i + \alpha_i) \quad (15)$$

This regularizer discourages overconfident estimates when prediction errors are large, implicitly encouraging the model to inflate uncertainty in regions of the input space where the prediction is uncertain or out-of-distribution. The total loss (\mathcal{L}_{ER}) for each training sample is a weighted sum of the two components:

$$\mathcal{L}_{\text{ER}} = \mathcal{L}_{\text{NLE}} + \lambda \cdot \mathcal{L}_{\text{Reg}} \quad (16)$$

where $\lambda \in \mathbb{R}_+$ is a hyperparameter controlling the trade-off between fitting the data and enforcing conservative uncertainty estimates [31].

3 Case Study

3.1 Problem Formulation

Condition-monitoring data typically comprises one-dimensional (1-D) vibrational signals acquired from multiple sensor channels. Consider a multivariate time series of observations,

$$\mathcal{X} = \{x_1, x_2, \dots, x_T\}, \quad x_t = [n_t^{(1)}, n_t^{(2)}, \dots, n_t^{(N_c)}]^\top, \quad (17)$$

where T denotes the total number of time steps and N_c denotes the number of channels. The objective is to train the PCNN to learn degradation mapping,

$$f: \underbrace{x_t, x_{t-1}, \dots, x_{t-\Delta t}}_{\text{input window}} \mapsto \hat{y}_t, \quad (18)$$

where $\Delta t \geq 0$ specifies the lookback window. When $\Delta t = 0$, the model ignores the temporal structure and reduces to pointwise regression:

$$\hat{y}_t = f(x_t). \quad (19)$$

In practice, degradation is governed by causal temporal dynamics: the evolution of system health depends on both current and preceding states. To reflect this, the degradation trajectory can be formulated as a discrete-time update,

$$\hat{y}_t = \hat{y}_{t-1} - g(x_t, x_{t-1}), \quad (20)$$

where $g(x_t, x_{t-1})$ represents the effective loss of health between successive timesteps. This formulation is intrinsically causal, relying only on the present observation x_t , the immediately preceding measurement x_{t-1} , and the prior estimate \hat{y}_{t-1} of remaining life.

3.2 Physics-Based Degradation Model for REBs

We develop a unified degradation model for REBs that captures fatigue, abrasive wear, lubrication breakdown, and stochastic contamination within a single coupled framework. Degradation is represented through coupled ordinary and stochastic differential equations, providing a coherent description of nonlinear progression over time. The total degradation is expressed as

$$\dot{D}_{\text{coupled}} = \dot{D}_F + \gamma_w \dot{D}_W + \zeta_L \dot{D}_O. \quad (21)$$

where D_F is fatigue degradation, D_W is the wear volume including surface roughness effects, and D_O represents lubrication degradation with thermal feedback. This formulation successfully captures the nonlinear dynamics of degradation and clearly describes three stages of bearing life: (i) Healthy, (ii) Fault Propagation, and (iii) Severe Fault. The evolution of these faults is illustrated in Figure 1. A full derivation and detailed explanation are provided in Appendix A.

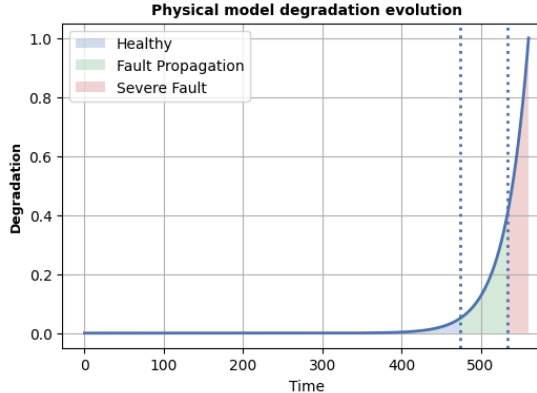


Figure 1: Fault evolution of physics-based degradation model.

3.3 Data, Curation, Evaluation Metrics, Training Strategy

Datasets: To test and benchmark the developed techniques, we utilize three publicly available datasets: (1) PRONOSTIA [37], (2) XJTU-SY [38], and (3) HUST [39]. Training was performed on the PRONOSTIA dataset, while cross-validation experiments were conducted on the other two datasets. For detailed dataset description refer to Appendix B.1.

Data curation: To extract physically meaningful degradation patterns, the raw signals are preprocessed into a time-frequency representation (TFR) following the methodology proposed in the authors' previous work [40]. For detailed preprocessing information refer to Appendix B.2.

Degradation labels: None of the datasets provides degradation labels. In the literature, two labeling strategies are commonly used for label generation: (1) linear and (2) piece-wise nonlinear. Both strategies were evaluated in this study. For PC-SNER, linear degradation assumption is adopted. For PC-SNGP, nonlinear and personalized degradation labels are generated by numerically solving Eqn. 21. For detailed description refer to Appendix B.2.1.

Evaluation metrics: Performance is evaluated using MSE, MAE, Score [37], and a new distance-aware coefficient (DAC) derived from the Pearson correlation coefficient (PCC) [41]. For detailed information refer to Appendix B.3.

PCNN training procedure: A custom PCNN training mechanism integrates all components within the PCNN framework. For detailed information, refer to Appendix B.4.

3.4 Computational Experiments

In this case study, the baseline PCNN architecture consists of six hidden layers, with the following configuration of neurons: [32, 32, 64, 64, 32, 32]. Each layer uses the *ReLU* as activation function. We evaluated the developed methods alongside a Monte Carlo dropout-based PCNN (PC-MC) [28] and Deep Ensemble (PC-DE) [42]. Both PC-MC and PC-DE are trained on linear degradation labels. For PC-SNGP, we consider the impact of the RBF kernel parameter γ in the covariance function of the GP output layer on the predictive performance and accuracy. Specifically, three values were tested: 0.5, 1.0, and 2.0. Similarly, for the PC-SNER approach, we investigated the influence of the regularization parameter λ , considering three values: 0.1, 0.2, and 0.5. In the case of the PC-MC, we explored the effect of applying dropout during inference, using three rates: 0.1, 0.2, and 0.3 after each hidden layer. For PC-DE, we consider the impact of the number of deep models: $N_m \in [10, 20, 30]$. For all developed models, we visualized (μ) along with respective uncertainty (aleatoric, epistemic, or both) bands extending up to 2σ , as well as contour plots, to facilitate comparison and analysis of the predictive behavior and uncertainty quantification. For the sake of explanation, we selected two test cases involving different bearings from Condition 1: one representing an \mathcal{X}_{IND} sample (Bearing 5) and another representing an \mathcal{X}_{OOD} sample (Bearing 1). The illustration results for \mathcal{X}_{IND} , and \mathcal{X}_{OOD} are provided in Figure 2 and Figure 3 with metrics results are summarized in Table 1, and Table 2, respectively.

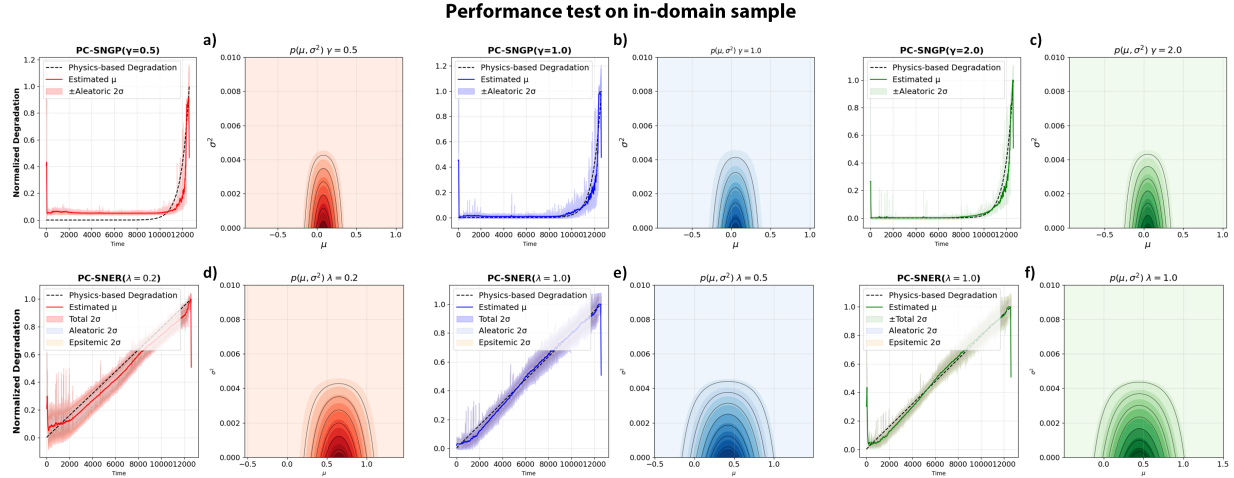


Figure 2: Results of the variation in the respective parameters for \mathcal{X}_{IND} sample.

Table 1: Summary of metric of performance test under \mathcal{X}_{IND} sample

| Model | MSE | MAE | Score | DAC |
|----------------------------|----------|----------|------------|--------|
| PC-SNGP($\gamma = 0.5$) | 0.006 58 | 0.062 47 | 74.072 10 | 0.1234 |
| PC-SNGP($\gamma = 1.0$) | 0.003 02 | 0.023 66 | 26.864 70 | 0.3188 |
| PC-SNGP($\gamma = 2.0$) | 0.002 04 | 0.016 35 | 17.357 78 | 0.2886 |
| PC-SNER($\lambda = 0.2$) | 0.003 02 | 0.049 27 | 49.214 65 | 0.0025 |
| PC-SNER($\lambda = 0.5$) | 0.000 71 | 0.018 18 | 19.326 06 | 0.4788 |
| PC-SNER($\lambda = 1.0$) | 0.001 41 | 0.020 78 | 23.123 72 | - |
| PC-MC($p_d = 0.1$) | 0.004 53 | 0.030 56 | 36.517 40 | - |
| PC-MC($p_d = 0.3$) | 0.030 29 | 0.114 36 | 145.911 67 | - |
| PC-MC($p_d = 0.5$) | 0.5488 | 0.5676 | 436.1328 | - |
| PC-DE($N_m = 10$) | 0.001 18 | 0.016 17 | 16.950 06 | - |
| PC-DE($N_m = 20$) | 0.000 90 | 0.022 56 | 22.199 14 | - |
| PC-DE($N_m = 30$) | 0.001 19 | 0.023 16 | 23.037 35 | - |

3.4.1 Performance on \mathcal{X}_{IND} sample

Figures 2(a–c) illustrate the effect of varying the γ parameter in PC-SNGP. At $\gamma = 0.5$, the model exhibits the highest uncertainty and achieves an MSE of 0.0065, an MAE of 0.0062, a score of 74.072, and a DAC of 0.1234. As γ increases, uncertainty decreases while distance awareness improves, yielding an MSE of 0.0030, an MAE of 0.0237, a score of 26.864, and a DAC of 0.31. When γ is further increased to 2.0, uncertainty continues to decrease; however, distance awareness slightly degrades, with an MSE of 0.00204, an MAE of 0.0163, a score of 17.35, and a DAC of 0.2886. Figures 2(d–f) illustrate the effects of varying the regularization parameter λ in PC-SNER. When $\lambda = 0.2$, the model exhibits the highest uncertainty, with an MSE of 0.0030, an MAE of 0.049, a score of 49.21, and a DAC of 0.0025. Increasing λ to 0.5 improves distance awareness, yielding an MSE of 0.00071, an MAE of 0.018, a score of 19.32, and a DAC of 0.4788. Further increasing λ to 1.0 results in a loss of distance-awareness capability, with an MSE of 0.00141, an MAE of 0.0207, a score of 23.13, and an undefined DAC. For PC-MC, at a dropout rate of $p_d = 0.1$, the model produces predictions with an MSE of 0.00453, an MAE of 0.03056, a score of 36.51, and an undefined DAC. When the dropout rate is increased to $p_d = 0.3$, the model performance deteriorates substantially, with the MSE increasing to 0.03029, the MAE to 0.11436, and the score to 145.91. This trend continues at $p_d = 0.5$, where the model becomes increasingly unstable. The performance metrics degrade sharply, with the MSE rising to 0.5488, the MAE to 0.5676, and the score to 436. For PC-DE with $N_m = 10$, the model achieves an MSE of 0.00118, an MAE of 0.01617, a score of 16.95, and an undefined DAC. Increasing N_m to 20 improves predictive performance, yielding an MSE of 0.0009, an MAE of 0.02256, and a score of 16.95. Further increasing N_m to 30 slightly degrades predictive accuracy, with an MSE of 0.00119, an MAE of 0.02316, and a score of 23.03.

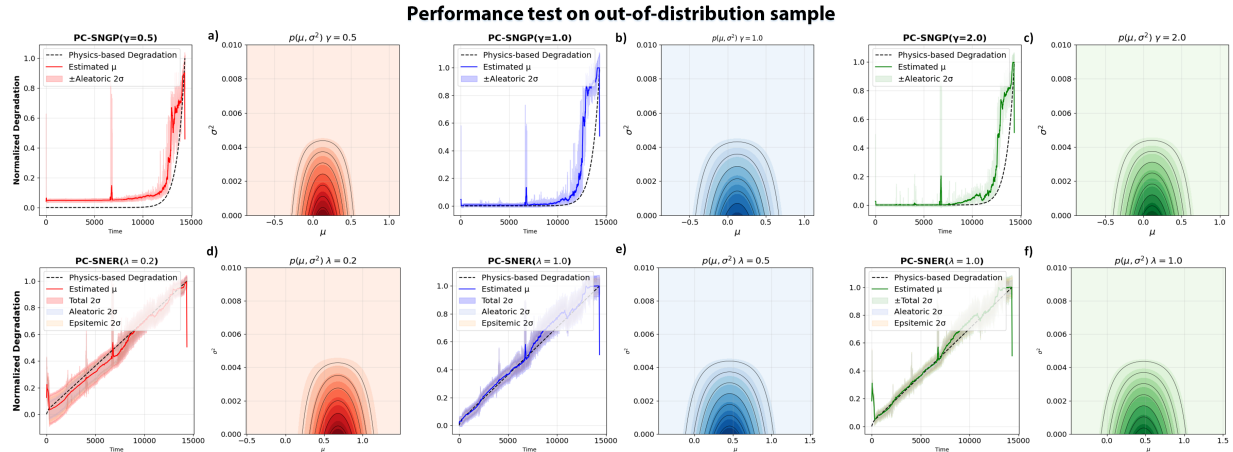


Figure 3: Results of the variation in the respective parameters for \mathcal{X}_{OOD} sample.

Table 2: Summary of metric generalization test under \mathcal{X}_{OOD} sample.

| Model | MSE | MAE | Score | DAC |
|----------------------------|---------|---------|----------|--------|
| PC-SNGP($\gamma = 0.5$) | 0.01285 | 0.08115 | 117.0852 | 0.3304 |
| PC-SNGP($\gamma = 1.0$) | 0.1160 | 0.07664 | 112.0871 | 0.4098 |
| PC-SNGP($\gamma = 2.0$) | 0.02062 | 0.06324 | 92.0488 | 0.3929 |
| PC-SNER($\lambda = 0.2$) | 0.00176 | 0.03212 | 36.6993 | - |
| PC-SNER($\lambda = 0.5$) | 0.00159 | 0.02807 | 39.5435 | 0.4744 |
| PC-SNER($\lambda = 1.0$) | 0.00190 | 0.02636 | 37.1943 | - |
| PC-MC($p_d = 0.1$) | 0.00684 | 0.04722 | 61.1557 | - |
| PC-MC($p_d = 0.3$) | 0.03370 | 0.10683 | 155.5201 | - |
| PC-MC($p_d = 0.5$) | 0.07143 | 0.19976 | 291.6539 | - |
| PC-DE($N_m = 10$) | 0.00168 | 0.03476 | 38.4916 | - |
| PC-DE($N_m = 20$) | 0.00204 | 0.03689 | 40.9841 | - |
| PC-DE($N_m = 30$) | 0.00121 | 0.02609 | 29.6929 | - |

3.4.2 Performance on \mathcal{X}_{OOD} sample

Figures 3(a–c) illustrate the performance of the PC-SNGP model under varying values of the γ parameter. At $\gamma = 0.5$ (Figure 3(a)), the model achieves its best overall performance with tight uncertainty bounds, yielding an MSE of 0.0128, an MAE of 0.081, a score of 117.08, and a DAC of 0.3304. At $\gamma = 1.0$, the uncertainty bounds widen; however, both accuracy and distance awareness improve, with an MSE of 0.0112, an MAE of 0.0766, a score of 112.08, and a DAC of 0.40. Further increasing γ to 2.0 slightly reduces uncertainty but leads to a degradation in accuracy, resulting in an MSE of 0.02, an MAE of 0.063, a score of 92, and a DAC of 0.39. Figures 3(d–f) present the results of the PC-SNER model under varying values of the regularization parameter λ . When $\lambda = 0.2$ (Figure 3(d)), the model exhibits relatively high uncertainty with moderate predictive performance and no distance-awareness capability, achieving an MSE of 0.0017, an MAE of 0.032, a score of 36.69, and an undefined DAC. Increasing λ to 0.5 (Figure 3(e)) substantially reduces uncertainty and improves model confidence, prediction accuracy, and distance awareness. This is reflected in a reduced MSE of 0.00159, a lower MAE of 0.028, a score of 39.54, and an increased DAC of 0.4744. However, further increasing λ to 1.0 (Figure 3(f)) leads to a degradation in overall performance, with the MSE rising to 0.0019, while the MAE and score decrease slightly to 0.02636 and 37.19, respectively, and the DAC becomes undefined. For PC-MC, at a dropout rate of $p_d = 0.1$, the model achieves an MSE of 0.0068, an MAE of 0.047, a score of 61.57, and an undefined DAC. Increasing the dropout rate to $p_d = 0.3$ leads to a significant degradation in performance, with the MSE rising to 0.071, the MAE to 0.106, and the score increasing to 155. This trend continues at $p_d = 0.5$, where the model becomes increasingly unstable, yielding an MSE of 0.7143, an MAE of 0.199, and a score of 291.65. For PC-DE, at $N_m = 10$, the model achieves an MSE of 0.0016, an MAE of 0.034, and a score of 38.49. Increasing N_m to 20 slightly degrades accuracy, with an MSE of 0.00204, an MAE of 0.03476, and a score of 38.49. Further increasing N_m to 30 improves performance, yielding an MSE of 0.00121, an MAE of 0.026, and a score of 29.69, while the DAC remains undefined across all configurations.

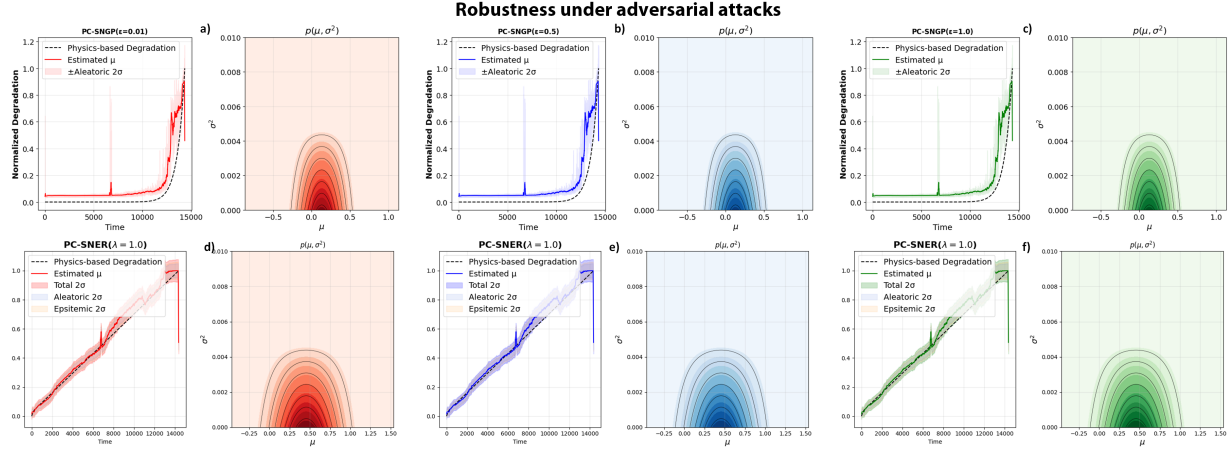
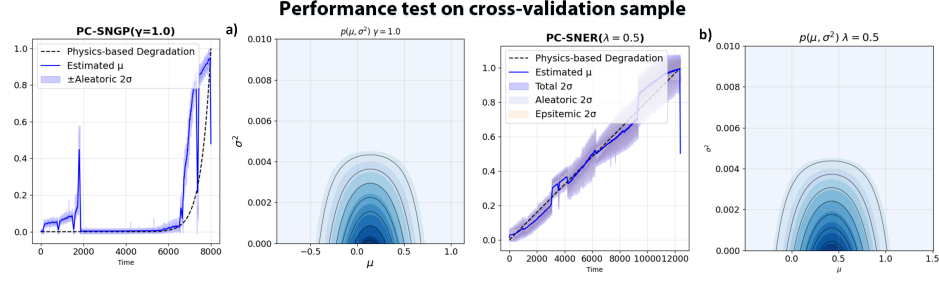


Figure 4: Results of the variation in the perturbation magnitude ϵ for \mathcal{X}_{OOD} sample.

Robustness under adversarial attacks: In the robustness evaluation, we assess the resilience of the developed methods under extreme scenarios, where OOD samples are subjected to adversarial attacks that potentially degrade model predictions and increase uncertainty. Adversarial examples are generated using the Fast Gradient Sign Method (FGSM) [43] with varying levels of perturbation magnitude $\epsilon \in \{0.01, 0.5, 1.0\}$. We employ the best performing configuration of both models – PC-SNGP ($\gamma = 1.0$) and PC-SNER ($\lambda = 0.5$). Figures 4(a–c) present the performance of the PC-SNGP model as ϵ increases, whereas Figures 4(d–f) depict the PC-SNER response for the same OOD example. The results demonstrate strong robustness to perturbations, with the uncertainty estimate remaining stable across increasing ϵ values. This is evident from the contour plots, which consistently focus around the predictive mean and show minimal variance. The observed robustness is attributed to two primary features of the developed design: (1) the Physics-constrained loss function, which imposes physical constraints that act as regularization, theREBs by suppressing overfitting and enhancing generalization; and (2) spectral normalization, which improves stability by constraining the model's Lipschitz constant [44], effectively limiting sensitivity to input perturbations.

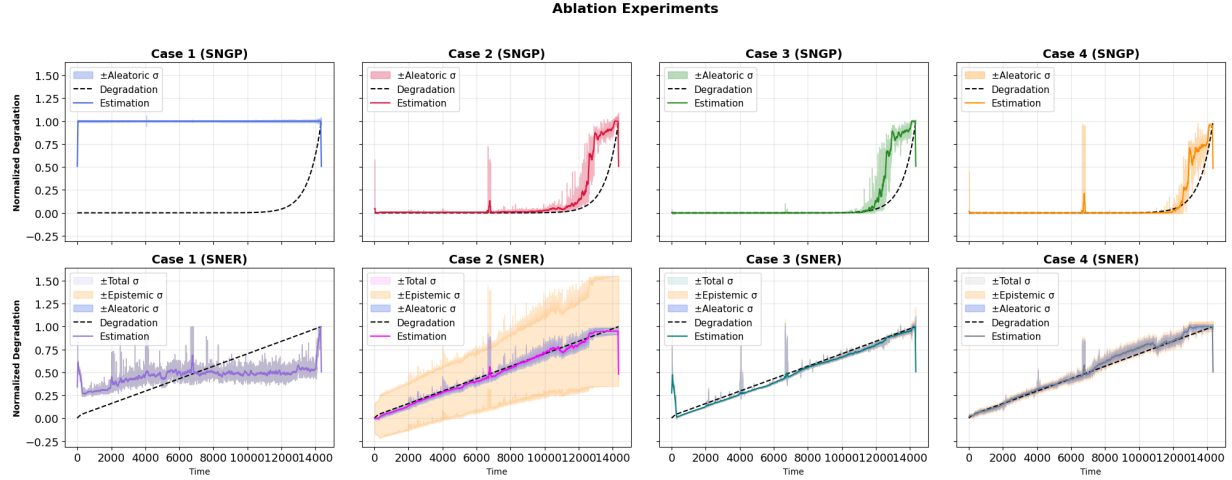
3.4.3 Performance on \mathcal{X}_{CV} samples

Cross-validation is essential in degradation estimation because it verifies that the predicted remaining life generalizes reliably to unseen data and novel degradation patterns. We conducted cross-validation experiments for PC-SNGP

Figure 5: Results of the \mathcal{X}_{CV} samples.Table 3: Summary of metrics cross-validation test under $\mathcal{X}_{\text{Cross-Val}}$ sample.

| Dataset | Model | MSE | MAE | Score | DAC |
|---------|---------|--------|--------|-------|------|
| XJTU-SY | PC-SNGP | 0.0319 | 0.0851 | 69.02 | 0.34 |
| HUST | PC-SNER | 0.0019 | 0.0337 | 37.54 | 0.12 |

using *Bearing 1* from Condition 1 of the XJTU-SY dataset, while cross-validation for PC-SNER was performed using *Bearing 1* from Condition 1 of the HUST dataset. The qualitative results are shown in Figure 5, and the quantitative metrics are summarized in Table 3. Both models demonstrate strong performance while preserving distance awareness. PC-SNGP achieves an MSE of 0.0319, an MAE of 0.0851, a score of 69.02, and a DAC of 0.34. PC-SNER achieves an MSE of 0.0019, an MAE of 0.0337, a score of 37.54, and a DAC of 0.12. These results indicate strong cross-validation capability and robustness of the developed approach.

Figure 6: Ablation Experiment results for \mathcal{X}_{OOD} sample.

3.5 Ablation Study

We conducted an ablation experiment to test and verify the contribution of each constituent in the developed models. These were modified into four cases. *Case 1*: without physics guidance. This was done to analyze the role and visualize the importance of physical knowledge in the convergence of NN. *Case 2*: without dynamic weights. This case was intended to demonstrate the impact of the dynamic weighting strategy on achieving a physically consistent model. *Case 3*: without spectral normalization. This case was designed to observe the effect of spectral normalization on uncertainty quantification and distance-awareness. *Case 4*: the complete model using the best-performing parameters—PC-SNGP ($\gamma = 1.0$) and PC-SNER ($\lambda = 0.5$). We utilized the same \mathcal{X}_{OOD} sample to conduct this test. Figure 6 presents the results of the ablation experiments, and the corresponding evaluation metrics are provided in Table 4.

Table 4: Summary metrics for ablation experiments under \mathcal{X}_{OOD} sample

| Model | Case | MSE | MAE | Score | DAC |
|---------|--------|----------|----------|------------|----------|
| PC-SNGP | Case 1 | 0.922 30 | 0.948 01 | 1428.79 | 0.337 88 |
| | Case 2 | 0.032 98 | 0.076 21 | 111.77 | 0.529 42 |
| | Case 3 | 0.033 21 | 0.066 83 | 98.013 | - |
| | Case 4 | 0.0116 | 0.076 | 112.08 | 0.4098 |
| PC-SNER | Case 1 | 0.056 53 | 0.202 16 | 252.639 54 | - |
| | Case 2 | 0.001 13 | 0.026 84 | 31.489 88 | - |
| | Case 3 | 0.003 20 | 0.036 62 | 42.597 36 | - |
| | Case 4 | 0.001 72 | 0.029 50 | 41.485 44 | 0.485 33 |

Figures 6(a-d) illustrate the outputs for the PC-SNGP models. In Case 1 (Figure 6(a)), the model failed to generalize due to underfitting, emphasizing the importance of physics guidance in achieving convergence towards an appropriate solution. The performance metrics for this case were: MSE = 0.922, MAE = 0.948, Score = 1428.79, and DAC = 0.337. In Case 2 (Figure 6(b)), the performance improved significantly relative to Case 1, although minor spikes were observed in the uncertainty bounds. The achieved metrics were: MSE = 0.03298, MAE = 0.07621, Score = 11.767, and DAC = 0.529. In Case 3 (Figure 6(c)), although the overall performance slightly degraded (MSE = 0.033, MAE = 0.0066, Score = 98.012), the DAC value became undefined, indicating that the model lost its distance-aware latent representation capabilities. In Case 4 (Figure 6(d)), the complete model exhibited the best performance with MSE = 0.0116, MAE = 0.0766, Score = 112.0, and DAC = 0.4098.

For the PC-SNER model (Figures 6(e-h)), a similar trend was observed: Case 4 consistently outperformed the others, while Case 1 performed the worst in both visual inspection and quantitative evaluation. It is important to note that all cases, except Case 4, lost the ability to preserve distance-aware capability in the latent space. From this ablation study, we conclude that incorporating physics guidance significantly enhances model convergence and accuracy. The dynamic weighting strategy, although a relatively subtle contribution, improves training stability and confidence. Spectral normalization is crucial for achieving distance-aware latent representations. The combination of these components yields the most reliable and physically consistent model performance.

3.6 Interpretability and Explanability

Although in AI systems higher predictive accuracy is often desirable, it does not necessarily imply that the underlying model provides a faithful representation of real-world degradation mechanisms. In many cases, such accuracy may be influenced by unintended biases introduced by specific features or a set of features. This underscores the importance of incorporating explainable AI (XAI) techniques within PHM systems. The objective of this experiment is to investigate the contribution of input features to the model's predictions, particularly in the context of potential over-reliance on key variables such as time (t) and temperature (T), which are explicitly incorporated into the loss. An overdependence on these variables could lead to biased predictions and reduced generalizability. To evaluate the feature importance and model behavior, we employ two model-agnostic XAI methods: Local Interpretable Model-Agnostic Explanations (LIME) [45] and SHapley Additive exPlanations (SHAP) [46].

The results for both PC-SNGP and PC-SNER are presented in Figure 7. For PC-SNGP (Figure 7(a-b)), the LIME analysis reveals that standard deviation (σ_h) contributes approximately 30% to the prediction, Energy (E_v) contributes around 17%, and time t contributes around 16%. The SHAP analysis reports mean SHAP values of 0.035 for σ_h , 0.025 for t , and 0.03 for T . Importantly, the remaining feature contributions are distributed across other input variables, suggesting a balanced utilization of the input space. A similar pattern is observed in the PC-SNER model (Figure 7(c-d)). Time (t) exhibits a 25% contribution with a mean SHAP value of 0.06, while temperature (T) contributes 17% with a mean SHAP value of 0.045. The remaining contribution is distributed among the other input features, with energy (E_v) emerging as a notably influential factor.

3.7 Interpreting the results

We observed that, for PC-SNGP, setting $\gamma = 1$ achieves a balance between uncertainty estimation and predictive performance. Larger values increase OOD uncertainty but degrade distance-aware calibration and accuracy. For PC-SNER, $\lambda = 0.5$ provides the optimal trade-off, minimizing predictive uncertainty while preserving meaningful distance-aware uncertainty estimates. Both proposed methods demonstrate strong resilience to noise and high accuracy in cross-validation experiments. LIME and SHAP analyses indicate that, although t and T are influential due to their

roles in the PC-loss formulation, the models do not rely excessively on them. Instead, they exploit a broader set of input features, supporting the interpretability and robustness of both methods.

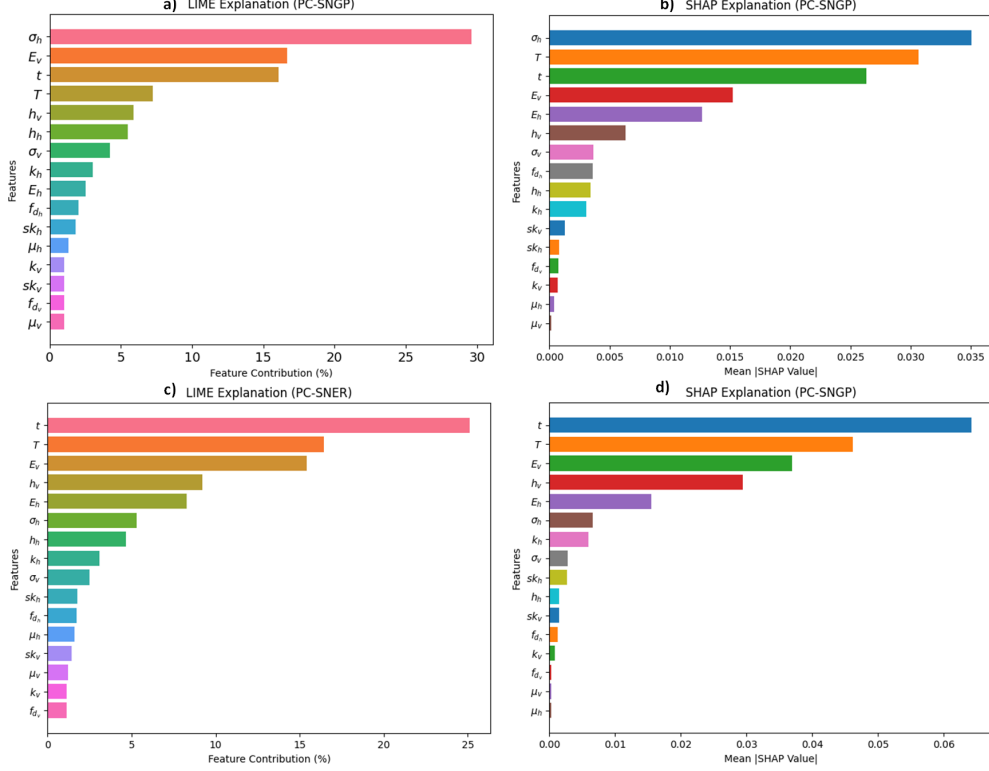


Figure 7: LIME and SHAP explanations for PC-SNGP(a-b) and PC-SNER(c-d).

4 Broader Impact

PCNNs have emerged as powerful tools for solving complex differential equations by embedding physical laws directly into the learning process. As these models are increasingly deployed in critical decision-making domains such as aerospace engineering [47], energy systems [48], robotics control [49], and biomedical applications [50], errors in prediction can lead to significant consequences. This necessitates the development of systematically calibrated uncertainty estimation methods within PCNNs to increase their reliability and safety.

This work contributes to the expanding body of research aimed at improving the accuracy, interpretability, and robustness of PCNNs. Rather than focusing solely on predictive performance, our approach augments PCNNs with the ability to quantify uncertainty in a distance-aware manner. This enhancement allows for more transparent and trustworthy predictions. Furthermore, the developed methods demonstrate strong resilience to noise, which is particularly important in real-world control systems where input perturbations are common and erroneous predictions can propagate through physical processes.

As trust in PCNNs increases, there is also a corresponding risk of overreliance on their outputs. This is especially concerning in high-stakes applications where human oversight remains essential. To mitigate this risk, incorporating redundancy, interpretability, and robust safety checks into PCNN-based systems is critical. Properly calibrated uncertainty estimates should not only enhance predictive performance but also highlight the limitations of the model, ultimately guiding responsible and informed decision-making.

5 Conclusion

In this work, we propose two uncertainty quantification methods for deterministic PCNNs: *PC-SNGP* and *PC-SNER*. Both methods enhance the capabilities of PCNNs not only by improving prediction accuracy but also by providing distance-aware, and evident estimates of predictive uncertainty. The methods begin by applying spectral normalization

to the weight matrices of the hidden layers up to the penultimate layer. In PC-SNGP, the standard dense output layer is replaced with a Gaussian Process to enable uncertainty estimation, which is sensitive to the distance between training and test samples. In PC-SNER, the output layer is modified to predict the parameters of a NIG distribution, allowing for direct and coherent estimation of uncertainty in a probabilistic framework. To assess the effectiveness of these methods, we employed several well-established performance metrics for evaluating prediction accuracy, along with distance-aware metric to analyze how uncertainty responds to the distance between test and training data. The developed methods were validated on the PRONOSTIA, XJTU-SY and HUST benchmark datasets for estimating the degradation of REBs. The results indicate that both methods outperform the MC Dropout and Deep-Ensemble approaches, achieving higher prediction accuracy and more reliable uncertainty quantification. The uncertainty estimates are low in regions near the training data and increase appropriately as the input moves further away, demonstrating good calibration. Additionally, both methods exhibit strong resilience to adversarial perturbations and noise.

Acknowledgments

This research was supported by the CAS-ANSO Scholarship. We acknowledge the intellectual and material contributions of the University of Science and Technology of China (USTC) and the Alliance of International Science Organizations (ANSO).

Ethics Approval

This study was conducted in accordance with ethical standards.

Data availability

The code will be available from corresponding author.

Authors Contribution

Waleed Razzaq: Conceptualization, Methodology, Data Curation, Writing- Original draft preparation. **Yun-Bo Zhao:** Supervision, Writing- Reviewing.

Conflict of interest

The authors declare that they have no known competing financial interests or personal relationships that could have appeared to influence the work reported in this paper.

References

- [1] Jakob Gawlikowski, Cedrique Rovile Njieutcheu Tassi, Mohsin Ali, Jongseok Lee, Matthias Humt, Jianxiang Feng, Anna Kruspe, Rudolph Triebel, Peter Jung, Ribana Roscher, et al. A survey of uncertainty in deep neural networks. *Artificial Intelligence Review*, 56(Suppl 1):1513–1589, 2023.
- [2] Yifei Ding, Minping Jia, Qiuhua Miao, and Peng Huang. Remaining useful life estimation using deep metric transfer learning for kernel regression. *Reliability Engineering & System Safety*, 212:107583, 2021.
- [3] Wei Guo, Hongrui Cao, Zhengjia He, and Laihao Yang. Fatigue life analysis of rolling bearings based on quasistatic modeling. *Shock and Vibration*, 2015(1):982350, 2015.
- [4] Alberto Gabrielli, Mattia Battarra, Emiliano Mucchi, and Giorgio Dalpiaz. Physics-based prognostics of rolling-element bearings: The equivalent damaged volume algorithm. *Mechanical Systems and Signal Processing*, 215:111435, 2024.
- [5] Hongxiang Yang, Yanxue Wang, Meng Li, and Meng Zhao. Rolling element load and path analysis in electromechanically coupled digital twin modeling of rotating machinery. *Measurement Science and Technology*, 2025.
- [6] Ravit Ohana, Omri Matania, Ariel Talan, Renata Klein, and Jacob Bortman. A new holistic approach to investigating and estimating rolling bearing rul based on physical grounds. *Structural Health Monitoring*, page 14759217251327357, 2025.

- [7] Lei Yang, Yibo Jiang, Kang Zeng, and Tao Peng. Rolling bearing remaining useful life prediction based on cnn-vae-mbilstm. *Sensors*, 24(10):2992, 2024.
- [8] Jingna Liu, Rujiang Hao, Qiang Liu, and Wenwu Guo. Prediction of remaining useful life of rolling element bearings based on lstm and exponential model. *International Journal of Machine Learning and Cybernetics*, 14(4):1567–1578, 2023.
- [9] Dong Guo, Zhi Cao, Hongyong Fu, and Zhenxiang Li. Remaining useful life estimation for rolling bearings using msgcnn-tr. *IEEE Sensors Journal*, 22(24):24333–24343, 2022.
- [10] Sunghyun Kim, Yun-Ho Seo, and Junhong Park. Transformer-based novel framework for remaining useful life prediction of lubricant in operational rolling bearings. *Reliability Engineering & System Safety*, 251:110377, 2024.
- [11] Guangjun Jiang, Zhengwei Duan, Qi Zhao, Dezhi Li, and Yu Luan. Remaining useful life prediction of rolling bearings based on tcn-msa. *Measurement Science and Technology*, 35(2):025125, 2023.
- [12] Junyu Qi, Rui Zhu, Chenyu Liu, Alexandre Mauricio, and Konstantinos Gryllias. Anomaly detection and multi-step estimation based remaining useful life prediction for rolling element bearings. *Mechanical Systems and Signal Processing*, 206:110910, 2024.
- [13] Jishnu Mukhoti, Andreas Kirsch, Joost van Amersfoort, Philip HS Torr, and Yarin Gal. Deep deterministic uncertainty: A new simple baseline. In *Proceedings of the IEEE/CVF Conference on Computer Vision and Pattern Recognition*, pages 24384–24394, 2023.
- [14] Tongyang Pan, Jinglong Chen, and Zijun Liu. A meta-weighted network equipped with uncertainty estimations for remaining useful life prediction of turbopump bearings. *Expert Systems with Applications*, 252:124161, 2024.
- [15] Zhiyuan Wu, Ning Liu, Guodong Li, Xinyu Liu, Yue Wang, and Lin Zhang. Learning adaptive probabilistic models for uncertainty-aware air pollution prediction. *IEEE Access*, 11:24971–24985, 2023.
- [16] Guang-Jun Jiang, Jin-Sen Yang, Tian-Cai Cheng, and Hong-Hua Sun. Remaining useful life prediction of rolling bearings based on bayesian neural network and uncertainty quantification. *Quality and Reliability Engineering International*, 39(5):1756–1774, 2023.
- [17] Andy Rivas, Gregory Kyriakos Delipei, and Jason Hou. Predictions of component remaining useful lifetime using bayesian neural network. *Progress in Nuclear Energy*, 146:104143, 2022.
- [18] Wanqing Song, Mingdeng Zhong, Minjie Yang, Deyu Qi, Simone Spadini, Piercarlo Cattani, and Francesco Villecco. Remaining useful life prediction of roller bearings based on fractional brownian motion. *Fractal and Fractional*, 8(4):183, 2024.
- [19] Sunday Ochella, Fateme Dimmohammadi, and Mahmood Shafiee. Bayesian neural networks for uncertainty quantification in remaining useful life prediction of systems with sensor monitoring. *Advances in Mechanical Engineering*, 16(7):16878132241239802, 2024.
- [20] Salvatore Cuomo, Vincenzo Schiano Di Cola, Fabio Giampaolo, Gianluigi Rozza, Maziar Raissi, and Francesco Piccialli. Scientific machine learning through physics-informed neural networks: Where we are and what's next. *Journal of Scientific Computing*, 92(3):88, 2022.
- [21] Manuel Arias Chao, Chetan Kulkarni, Kai Goebel, and Olga Fink. Fusing physics-based and deep learning models for prognostics. *Reliability Engineering & System Safety*, 217:107961, 2022.
- [22] Chen Yin, Yuqing Li, Yulin Wang, and Yining Dong. Physics-guided degradation trajectory modeling for remaining useful life prediction of rolling bearings. *Mechanical Systems and Signal Processing*, 224:112192, 2025.
- [23] Kai Zhou and Jiong Tang. A wavelet neural network informed by time-domain signal preprocessing for bearing remaining useful life prediction. *Applied Mathematical Modelling*, 122:220–241, 2023.
- [24] Yigit A Yucesan and Felipe AC Viana. Hybrid physics-informed neural networks for main bearing fatigue prognosis with visual grease inspection. *Computers in Industry*, 125:103386, 2021.
- [25] Wenjian Lu, Yu Wang, Mingquan Zhang, and Junwei Gu. Physics guided neural network: Remaining useful life prediction of rolling bearings using long short-term memory network through dynamic weighting of degradation process. *Engineering Applications of Artificial Intelligence*, 127:107350, 2024.
- [26] HU Yong, CHAO Qun, XIA Pengcheng, and LIU Chengliang. Remaining useful life prediction using physics-informed neural network with self-attention mechanism and deep separable convolutional network. *Journal of Advanced Manufacturing Science and Technology*, 4(4), 2024.

[27] Kevin Linka, Amelie Schäfer, Xuhui Meng, Zongren Zou, George Em Karniadakis, and Ellen Kuhl. Bayesian physics informed neural networks for real-world nonlinear dynamical systems. *Computer Methods in Applied Mechanics and Engineering*, 402:115346, 2022.

[28] Mohammed S Alhajeri, Fahim Abdullah, Zhe Wu, and Panagiotis D Christofides. Physics-informed machine learning modeling for predictive control using noisy data. *Chemical Engineering Research and Design*, 186:34–49, 2022.

[29] Jerol Soibam, Ioanna Aslanidou, Konstantinos Kyriyanidis, and Rebei Bel Fdhila. Inverse flow prediction using ensemble pinns and uncertainty quantification. *International Journal of Heat and Mass Transfer*, 226:125480, 2024.

[30] Jeremiah Liu, Zi Lin, Shreyas Padhy, Dustin Tran, Tania Bedrax Weiss, and Balaji Lakshminarayanan. Simple and principled uncertainty estimation with deterministic deep learning via distance awareness. *Advances in neural information processing systems*, 33:7498–7512, 2020.

[31] Alexander Amini, Wilko Schwarting, Ava Soleimany, and Daniela Rus. Deep evidential regression. *Advances in neural information processing systems*, 33:14927–14937, 2020.

[32] Takeru Miyato, Toshiki Kataoka, Masanori Koyama, and Yuichi Yoshida. Spectral normalization for generative adversarial networks. *arXiv preprint arXiv:1802.05957*, 2018.

[33] A Llera and CF Beckmann. Estimating an inverse gamma distribution. *arXiv preprint arXiv:1605.01019*, 2016.

[34] Andrey Malinin and Mark Gales. Reverse kl-divergence training of prior networks: Improved uncertainty and adversarial robustness. *Advances in neural information processing systems*, 32, 2019.

[35] Andrey Malinin and Mark Gales. Predictive uncertainty estimation via prior networks. *Advances in neural information processing systems*, 31, 2018.

[36] Jayaram Sethuraman. A constructive definition of dirichlet priors. *Statistica sinica*, pages 639–650, 1994.

[37] Patrick Nectoux, Rafael Gouriveau, Kamal Medjaher, Emmanuel Ramasso, Brigitte Chebel-Morello, Noureddine Zerhouni, and Christophe Varnier. Pronostia: An experimental platform for bearings accelerated degradation tests. In *IEEE International Conference on Prognostics and Health Management, PHM'12.*, pages 1–8. IEEE Catalog Number: CPF12PHM-CDR, 2012.

[38] Biao Wang, Yaguo Lei, Naipeng Li, et al. Xjtu-sy bearing datasets. *GitHub, GitHub Repository*, 2018.

[39] Nguyen Duc Thuan and Hoang Si Hong. Hust bearing: a practical dataset for ball bearing fault diagnosis. *BMC research notes*, 16(1):138, 2023.

[40] Waleed Razzaq and Yun-Bo Zhao. Carle: a hybrid deep-shallow learning framework for robust and explainable rul estimation of rolling element bearings. *Soft Computing*, 29(23):6269–6292, 2025.

[41] Israel Cohen, Yiteng Huang, Jingdong Chen, Jacob Benesty, Jacob Benesty, Jingdong Chen, Yiteng Huang, and Israel Cohen. Pearson correlation coefficient. *Noise reduction in speech processing*, pages 1–4, 2009.

[42] Balaji Lakshminarayanan, Alexander Pritzel, and Charles Blundell. Simple and scalable predictive uncertainty estimation using deep ensembles. *Advances in neural information processing systems*, 30, 2017.

[43] Yujie Liu, Shuai Mao, Xiang Mei, Tao Yang, and Xuran Zhao. Sensitivity of adversarial perturbation in fast gradient sign method. In *2019 IEEE symposium series on computational intelligence (SSCI)*, pages 433–436. IEEE, 2019.

[44] Henry Gouk, Eibe Frank, Bernhard Pfahringer, and Michael J Cree. Regularisation of neural networks by enforcing lipschitz continuity. *Machine Learning*, 110:393–416, 2021.

[45] Marco Tulio Ribeiro, Sameer Singh, and Carlos Guestrin. " why should i trust you?" explaining the predictions of any classifier. In *Proceedings of the 22nd ACM SIGKDD international conference on knowledge discovery and data mining*, pages 1135–1144, 2016.

[46] Scott M Lundberg and Su-In Lee. A unified approach to interpreting model predictions. *Advances in neural information processing systems*, 30, 2017.

[47] Alice Inbaraj. Physics-informed neural networks for trajectory prediction and uncertainty quantification in urban air mobility. Master's thesis, San Diego State University, 2025.

[48] Yuantao Yao, Te Han, Jie Yu, and Min Xie. Uncertainty-aware deep learning for reliable health monitoring in safety-critical energy systems. *Energy*, 291:130419, 2024.

[49] Eunho Lee and Hyunseok Yang. Uampnet: Uncertainty-aware motion planning network for manipulator motion planning. *IEEE Access*, 2024.

- [50] Mario De Florio, Zongren Zou, Daniele E Schiavazzi, and George Em Karniadakis. Quantification of total uncertainty in the physics-informed reconstruction of cvsim-6 physiology. *Philosophical Transactions A*, 383(2292):20240221, 2025.
- [51] Eliahu Zahavi. *Fatigue design: life expectancy of machine parts*. CRC press, 2019.
- [52] JJ Kauzlarich and JA Williams. Archard wear and component geometry. *Proceedings of the Institution of Mechanical Engineers, Part J: Journal of Engineering Tribology*, 215(4):387–403, 2001.
- [53] Micha Peleg, Mark D Normand, and Maria G Corradini. The arrhenius equation revisited. *Critical reviews in food science and nutrition*, 52(9):830–851, 2012.
- [54] Luís Aguiar-Conraria and Maria Joana Soares. The continuous wavelet transform: Moving beyond uni-and bivariate analysis. *Journal of economic surveys*, 28(2):344–375, 2014.
- [55] Richard Büssow. An algorithm for the continuous morlet wavelet transform. *Mechanical Systems and Signal Processing*, 21(8):2970–2979, 2007.
- [56] Baoping Tang, Wenyi Liu, and Tao Song. Wind turbine fault diagnosis based on morlet wavelet transformation and wigner-ville distribution. *Renewable Energy*, 35(12):2862–2866, 2010.
- [57] Jun Zhu, Nan Chen, and Weiwen Peng. Estimation of bearing remaining useful life based on multiscale convolutional neural network. *IEEE Transactions on Industrial Electronics*, 66(4):3208–3216, 2018.

Appendix

A Physics-based Degradation Model

We develop a unified degradation model for REBs that captures fatigue, abrasive wear, lubrication breakdown, and stochastic contamination within a single coupled framework. Degradation is represented through coupled ordinary and stochastic differential equations, providing a coherent description of nonlinear progression over time. The model variables are:

- P : radial load on the bearing (N).
- n : rotational speed (RPM), ω : angular speed (rad/s).
- C_{load} : nominal dynamic load rating (N)
- $C_{\text{eff}}(t)$: time-varying effective load rating (N) coupling all degradation mechanisms.
- $D_W(t)$: accumulated wear volume (m^3)
- $V_d(t)$: equivalent damaged volume for fatigue (m^3).
- $R(t)$: surface roughness metric.
- $O(t)$: lubricant oxidation state (dimensionless index, e.g., normalized TAN)
- $\nu(t)$: lubricant kinematic viscosity (Pa·s).
- $C_{\text{debris}}(t)$: debris concentration (particles per unit volume).
- \mathcal{W}_t : standard Wiener process representing stochastic contamination.
- $D_{\text{coupled}}(t)$: cumulative damage index (dimensionless).

A.1 Components model and Physical Rationale

A.1.1 Fatigue: Hertzian contact, Lundberg–Palmgren scaling, and EDV

Fatigue in REBs arises from subsurface shear stresses induced by repeated Hertzian contact, where material failure reflects the gradual accumulation of microstructural damage. Classical fatigue models capture this process through probabilistic cycle counting [51], but neglect how the stressed material volume and structural capacity evolve as damage develops. We address this limitation by combining Hertzian elastomechanics, which govern the load- and curvature-dependent behavior of the subsurface stress field, with an Equivalent Damaged Volume (EDV) formulation that links geometry, stress, and microstructural evolution. In this framework, fatigue is governed by the growth of a representative damaged volume $V_d(t)$ under repetitive loading, making the degradation rate explicitly dependent on prior damage and on load-dependent weakening through a time-varying effective load rating $C_{\text{eff}}(t)$, the REBs capturing the progressive reduction in bearing capacity preceding macroscopic crack formation.

The Hertzian peak pressure for a ball contact is given by

$$\sigma_H = \sqrt[3]{\frac{6P(E^*)^2}{\pi^3(R^*)^2}}, \quad (22)$$

which sets characteristic subsurface stress magnitudes. The baseline L–P damage intensity in seconds (cycles^{−1}) under current capacity $C_{\text{eff}}(t)$ is

$$k_f(t) = \left(\frac{P}{C_{\text{eff}}(t)} \right)^p \frac{n}{60 \times 10^6}, \quad (23)$$

with $p \approx 3$ for balls (or empirical alternative for rollers). To account for prior damage, we add an EDV term. For lumped modeling, the EDV growth rate is approximated as

$$\frac{dV_d}{dt} \approx \phi \left(\frac{P}{C_{\text{eff}}(t)} \right)^q n, \quad (24)$$

with $q > p$ reflecting the stronger sensitivity of damaged volume to contact stress peaks; ϕ is calibrated. The combined instantaneous fatigue damage rate is

$$\frac{dD_F}{dt} = k_f(t) + \beta \frac{dV_d}{dt} = \left(\frac{P}{C_{\text{eff}}(t)} \right)^p \frac{n}{60 \times 10^6} + \beta \phi \left(\frac{P}{C_{\text{eff}}(t)} \right)^q n. \quad (25)$$

This form retains the empirical foundation of L–P while introducing a physically motivated, damage-accelerating EDV correction. The EDV term is small early in life ($\beta\phi \ll 1$) and can dominate as $C_{\text{eff}}(t)$ declines.

A.1.2 Wear and Surface Roughness: Extended Archard with feedback

Wear originates from sliding or rolling contact between surface asperities and is classically described by Archard's law [52], which relates material loss to applied load, sliding distance, and hardness, but assumes fixed surface conditions. To capture the feedback mechanism observed in practice, we extend this framework by introducing surface roughness $R(t)$ as an internal state variable and by accounting for debris-induced abrasion. As roughness increases, local contact pressure peaks intensify. Brittle micro-asperities fracture more readily, accelerating wear. At the same time, generated debris acts as a third-body abrasive cycle in which wear drives roughening and roughening accelerates wear, captured through a time-dependent wear modification factor $W_{\text{mod}}(t)$ that reduces the $C_{\text{eff}}(t)$ as the surface progressively departs from its original geometry.

The wear volume rate is given by

$$\frac{dD_W}{dt} = \frac{A_v P}{H_{\text{hard}}} \frac{ds}{dt} + A_a R(t), \quad (26)$$

where A_v is the Archard wear coefficient, H_{hard} is the material hardness, ds/dt is the sliding speed, and A_a scales roughness-driven abrasive loss. Surface roughness evolves according to

$$\frac{dR}{dt} = \gamma_r \frac{dD_W}{dt} + \delta_c C_{\text{debris}}(t), \quad (27)$$

where γ_r links volume loss to roughness growth and δ_c captures contamination-induced roughening due to debris particles. A geometric degradation modifier is introduced to reduce the effective load-carrying capacity as the surface departs from its nominal geometry,

$$W_{\text{mod}}(t) = (1 + \eta V(t) + \zeta R(t)^2)^{-1}. \quad (28)$$

This modifier is bounded such that $0 < W_{\text{mod}} \leq 1$, penalizing both bulk material loss and amplified asperity-level stress.

A.1.3 Lubricant Oxidation and Thermal Feedback

Lubricant degradation in rolling element bearings is governed by thermally activated oxidative reactions that break down long-chain molecules, leading to a progressive loss of viscosity that follows Arrhenius kinetics and accelerates at elevated temperature [53]. We model this process by coupling chemical depletion, thermal effects, and tribological response. Oxidation consumes a finite chemical reservoir O_{max} , reducing viscosity and thinning the lubricant film that separates the rolling elements from the raceways. The resulting viscosity loss increases frictional dissipation, which raises the operating temperature and further accelerates oxidation, forming a positive thermal feedback that can trigger runaway degradation under high load or insufficient cooling. By embedding these interactions within the thermal balance equation, the formulation captures how lubrication failure degrades load-carrying capacity and amplifies fatigue and wear processes.

The oxidation state is modeled using first-order Arrhenius kinetics, approaching a saturation level O_{max} ,

$$\frac{dO}{dt} = k_o (O_{\text{max}} - O) \cdot e^{\left(-\frac{E_a}{k_B T(t)}\right)}. \quad (29)$$

Kinematic viscosity decays with oxidation according to an empirical

$$\nu(t) = \nu_0 \cdot e^{\left(-\alpha O(t) - \frac{E_{\text{vis}}}{k_B T(t)} + \frac{E_{\text{vis}}}{k_B T_0}\right)} \quad (30)$$

Here, E_{vis} is the activation energy for viscous flow (typically 20-40 kJ/mol for mineral oils, calibrated from lubricant datasheets showing viscosity-temperature curves), and T_0 is a reference temperature (e.g., 313 K or 40°C). A lumped balance model of thermal dynamics:

$$\frac{dD_O}{dt} = \frac{1}{mc_p} \left[\mu_f P \omega - hA(T - T_a) + \xi \frac{dO}{dt} \right], \quad (31)$$

where mc_p is the effective thermal mass, μ_f is the friction coefficient, which may be modeled as a function of viscosity in refined formulations, hA is the effective heat transfer coefficient, and η represents the exothermic contribution of oxidation reactions. The coupling is two-way: temperature T controls the oxidation rate, oxidation reduces viscosity, and reduced viscosity increases frictional heating.

A.1.4 Stochastic Micro-Contamination

Contamination strongly accelerates bearing degradation, yet its evolution is inherently random due to particles originating from external ingress, internally generated wear debris, and intermittent release events associated with surface fracture. These contamination bursts exhibit non-Gaussian intermittent behavior that cannot be represented by deterministic dynamics. We therefore model debris concentration using a stochastic differential equation driven by a Wiener process, where the drift term captures deterministic generation from wear, and the diffusion term represents random fluctuations in particle generation, transport, agglomeration, and detachment. This stochastic formulation reflects variability arising from irregular operating conditions and lubricant flow instability, and captures the empirically observed burst-like increase in contamination that alters surface roughness, modifies contact mechanics, and rapidly accelerates fatigue progression.

Debris accumulation is modeled as a stochastic process to reflect bursty particle transport.

$$dC_{debris}(t) = \rho \frac{dD_W}{dt} dt + \sigma_c d\mathcal{W}_t. \quad (32)$$

where ρ converts wear volume rate to particle concentration rate and σ_c scales the noise intensity. This SDE produces sample paths with random spikes that match observed contamination bursts.

A.1.5 Effective Load Rating and Mechanistic Coupling

The effective load rating $C_{\text{eff}}(t)$ provides a unifying state variable that couples the model's four degradation pathways by allowing load-carrying capacity to evolve rather than remain static. Unlike classical rating, this formulation reflects how capacity degrades as lubrication deteriorates, surfaces wear, and contaminants accumulate. Lubricant breaks down the thin film, increasing contact stresses and accelerating fatigue, while wear-induced geometric distortion reduces contact conformity and amplifies local stress concentration. Contamination further intensifies abrasion and disrupts lubricant films, compounding both wear and fatigue. The combined effect is a dynamically shrinking $C_{\text{eff}}(t)$ that drives nonlinear acceleration of damage near end-of-life, consistent with field observations: slow early degradation followed by rapid failure.

The effective load rating couples the four degradation processes:

$$C_{\text{eff}}(t) = C_{\text{load}} \cdot L_{\text{life}}(t, T) \cdot W_{\text{mod}}(t) \cdot e^{(-\psi C_{\text{debris}}(t))}, \quad (33)$$

where the lubrication life factor is

$$L_{\text{life}}(t, T) = \frac{\nu(t)}{\nu_0}. \quad (34)$$

Total degradation is

$$\frac{dD_{\text{coupled}}}{dt} = \frac{dD_F}{dt} + \gamma_w \frac{dD_W}{dt} + \zeta_L \frac{dD_O}{dt}. \quad (35)$$

B Data, Curation, Evaluation Metrics, Training Strategy

B.1 Dataset Explanation

PRONOSTIA: dataset is a widely used benchmark in the field of condition monitoring and degradation estimation of REBs. Developed by Nectoux et al. [37] as part of the PRONOSTIA experimental platform, the dataset comprises 17 complete run-to-failure experiments conducted under accelerated wear conditions across three distinct operating regimes: 1800 rpm with a 4 kN radial load, 1650 rpm with a 4.2 kN load, and 1500 rpm with a 5 kN load, all recorded at a frequency of 100 Hz. Vibration data were captured via accelerometers mounted along both the horizontal and vertical axes and sampled at 25.6 kHz. Additionally, temperature measurements were recorded at a rate of 10 Hz. To train the models, we utilized data from four bearings ($4 \sim 7 \in \mathcal{X}_{\text{IND}}$) operating under 100Hz4kN, incorporating both vibration and temperature data. To evaluate the model's generalization performance on \mathcal{X}_{OOD} , the remaining bearings from all operating conditions were utilized. The summary of the dataset characteristics and distribution is provided in Table 5.

XJTU-SY: dataset is a publicly available benchmark for degradation estimation of REBs. It was developed by Xi'an Jiaotong University in collaboration with Changxing Sumyoung Technology Company. The dataset consists of 15 complete run-to-failure experiments conducted under three operating conditions, defined by different combinations of rotational speed and radial load: 2100 rpm with a 12 kN load, 2250 rpm with an 11 kN load, and 2400 rpm with a 10 kN load. Vibration signals were collected using accelerometers mounted in both horizontal and vertical directions and sampled at 25.6 kHz. This dataset is used only for cross-validation results.

Table 5: Data distributions of PRONOSTIA, XJTU-SY, and HUST datasets.

| Dataset | Condition | Frequency | Radial Load | Speed | \mathcal{X}_{IND} | $\mathcal{X}_{OOD/CV}$ |
|-----------|-------------|-----------|-------------|----------|---------------------|------------------------|
| PRONOSTIA | Condition 1 | 100 Hz | 4 kN | 1800 rpm | 4 ~ 7 | 1 ~ 3 |
| | Condition 2 | 100 Hz | 4.2 kN | 1650 rpm | - | 1 ~ 7 |
| | Condition 3 | 100 Hz | 5 kN | 1500 rpm | - | 1 ~ 3 |
| XJTU-SY | Condition 1 | 35 Hz | 4 kN | 2100 rpm | - | 1 ~ 5 |
| | Condition 2 | 37.5 Hz | 4.2 kN | 2250 rpm | - | 1 ~ 5 |
| | Condition 3 | 40 Hz | 5 kN | 2400 rpm | - | 1 ~ 5 |
| HUST | Condition 1 | - | 0 W | - | - | 1 ~ 5 |
| | Condition 2 | - | 200 W | - | - | 1 ~ 5 |
| | Condition 3 | - | 400 W | - | - | 1 ~ 5 |

Note: The PRONOSTIA dataset is utilized for training and generalization testing, while the XJTU-SY and HUST datasets are employed to evaluate cross-validation testing. (-) values are either not available or not utilized.

HUST: dataset was developed by Huazhong University of Science and Technology using a dedicated accelerated life test platform. The dataset comprises five bearings tested under three different load conditions: 0 W, 200 W, and 400 W. Vibration signals were acquired using accelerometers mounted along the horizontal and vertical directions and sampled at 25.6 kHz. Data were recorded continuously throughout the bearing lifecycle until failure, providing complete degradation trajectories. This dataset is used only for cross-validation experiments.

B.2 Data Curation

The condition monitoring data of rotating machinery typically comprises 1-D nonstationary vibration signals acquired from multiple sensors. To facilitate time–frequency analysis, the raw signals $x(t)$ are first segmented using a time-based rectangular windowing function $w(t)$, allowing improved localization of transient features across the time and frequency domains. Each segmented signal $x_w(t) = x(t) \cdot w(t)$ is then subjected to a continuous wavelet transform (CWT) [54] using the Morlet wavelet [55] $\psi(t)$ as the mother wavelet. The Morlet wavelet is selected because it resembles the impulse response of localized bearing faults [56, 57], which enhances sensitivity to fault-induced transients [40]. The CWT is defined as:

$$W(a, b) = \int_{-\infty}^{\infty} x_w(t) \frac{1}{\sqrt{a}} \psi^* \left(\frac{t-b}{a} \right) dt, \quad (36)$$

where a and b denote the scale and translation parameters, respectively. From the resulting time–frequency representation (TFR), a set of statistical and domain-relevant features is extracted to characterize the bearing’s operational condition. These features are computed in both the time and frequency domains and are selected to maintain physical interpretability while maximizing discriminative power. A detailed summary of all the extracted features, their mathematical formulations, and their physical significance is provided in Table 6. Algorithm 1 provides the full method for extracting the TFR features.

B.2.1 Degradation labels

Accurate real-world RUL distribution is a critical step in developing effective RUL estimation models. In the literature, two main approaches are commonly studied: (i) assuming a constant degradation rate, and (ii) modeling piecewise nonlinear degradation patterns. To capture both perspectives, we generate linear monotonic degradation labels for PC-SNER, from 0 to 1, where 0 denotes the optimal state, and 1 indicates the end of life (EOL). For PC-SNGP, we numerically solve the Eqn. 21 using the Runge–Kutta method. The resulting labels are then normalized to the range [0, 1]. This approach enables more accurate and individualized EOL estimation for each bearing while remaining physically consistent. The illustrations of both labels are provided in Figure 8.

B.3 Evaluation Metrics

In this study, we first evaluate the prediction accuracy of the developed approaches using commonly employed metrics such as mean squared error (MSE), mean absolute error (MAE), and the Score [37]. Existing metrics for evaluating uncertainty in deep learning models, including negative log-likelihood (NLL) and root mean square calibration error (RMSCE), primarily assess overall predictive uncertainty and the model’s confidence in its predictions. However, in safety-critical and risk-sensitive applications, such as degradation estimation, it is essential that the model’s predictive uncertainty effectively informs decision-makers about the reliability of predictions, particularly regarding potential failures. Therefore, we propose a distance-aware calibration performance metric.

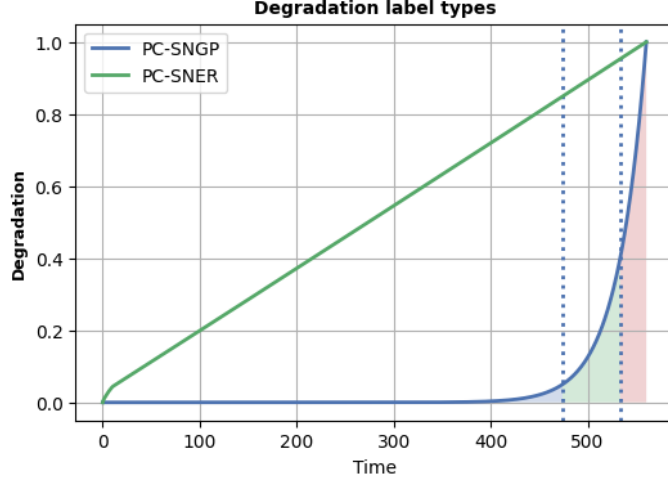


Figure 8: Degradation labels

Table 6: Summary of time–frequency features, formulas, domains, and physical meanings

| Feature | Formula | Domain | Physical Meaning |
|---|---|-----------|--|
| Energy (E) | $E = \sum_{m=1}^M \Gamma_i(a, b) ^2$ | Frequency | Measures vibrational activity. Increases suggest wear or defects (e.g., spalling). |
| Dominant Frequency (f_d) | $f_d = a_{\text{scale}}(\text{argmax}(E))$ | Frequency | Identifies frequency with the highest energy, which is useful for detecting faults such as bearing cracks. |
| Entropy (h) | $h = - \sum_{i=1}^K P(i) \log P(i)$ | Time | Quantifies randomness in vibrations. Higher values indicate irregular defects or friction. |
| Kurtosis (K) | $K = \frac{\mathbb{E}[(i-\mu)^4]}{\sigma^4}$ | Time | Detects extreme signal spikes. High values indicate localized defects (e.g., cracks). |
| Skewness (s_k) | $s_k = \frac{\mathbb{E}[(i-\mu)^3]}{\sigma^3}$ | Time | Measures signal asymmetry. Positive skew suggests unidirectional impacts, negative skew suggests crack initiation. |
| Mean (μ) | $\mu = \frac{1}{N} \sum_{m=1}^M i(m)$ | Time | Baseline vibrational level. Increases suggest wear or faults (e.g., cage failure). |
| Standard Deviation (σ) | $\sigma = \sqrt{\frac{1}{M} \sum_{i=1}^m (i(m) - \mu)^2}$ | Time | Measures signal variability. High values indicate instability or faults such as looseness or contamination. |

Consider a predictive distribution $p(y|x)$ trained on \mathcal{X}_{IND} , where $(\|\cdot\|_x)$ denotes the input data manifold equipped with an appropriate metric. We define $p(y|x)$ as input distance-aware if there exists a summary statistic $a(x)$ of the predictive distribution that quantifies uncertainty in a manner that reflects the distance between the test input x and the training data manifold:

$$a(x) = g_m(d(x, \mathcal{X}_{\text{IND}})), \quad (37)$$

where g_m is a monotonic function and $d(x, \mathcal{X}_{\text{IND}}) = \mathbb{E}_{x' \sim \mathcal{X}_{\text{IND}}} [\|x - x'\|_x]$ represents the expected distance from x to \mathcal{X}_{IND} calculated using Euclidean distance. To measure the sensitivity of the quantified uncertainty with respect to this distance, we introduce the distance-aware coefficient (DAC), defined as the Pearson correlation coefficient [41] between

Algorithm 1 Time–frequency representation extraction algorithm

Require: windowed signal I_w , critical frequency f_c , operating frequency f_o , sampling period $T_{sampling}$, windowed physical constraints (t_w, T_w)

- 1: $a_{min} = \frac{f_c}{f_{max} \cdot T_{sampling}}$, $a_{max} = \frac{f_c}{f_{min} \cdot T_{sampling}}$,
- 2: $a_{scale} \in [a_{min}, a_{max}]$
- 3: $I_{TFR} \leftarrow \{\}$
- 4: **for** (i_w, t_n, T_n) in (I_w, t_w, T_w) : **do**
- 5: Compute wavelets as: $\Gamma_{iw}(a, b) = \int_{-\infty}^{\infty} i_w \psi^* \left(\frac{t-b}{a} \right) dt$.
- 6: Compute Energy as: $E = \sum_{m=1}^M |\Gamma_{iw}(a, b)|^2$
- 7: Compute Dominant frequency as: $f_d = a_{scale} [\arg \max(E)]$.
- 8: Compute Entropy as: $h = - \sum_{i=m}^M P(i_w(t)) \log P(i_w(t))$.
- 9: Compute Kurtosis as: $K = \frac{\mathbb{E}[(i_w(t) - \mu)^4]}{\sigma^4}$.
- 10: Compute Skewness as: $sk = \frac{\mathbb{E}[(i_w(t) - \mu)^3]}{\sigma^3}$.
- 11: Compute mean as: $\mu = \frac{1}{M} \sum_{m=1}^M i_w(m)$.
- 12: Compute standard deviation as: $\sigma = \sqrt{\frac{1}{M} \sum_{i=1}^M (i_w(m) - \mu)^2}$.
- 13: $X_n \leftarrow [\log(E), f_d, h, K, sk, \mu, \sigma]$
- 14: **end for**
- 15: **return** $I_{TFR} = \text{Concat}(X_1, X_2 \dots X_{N_s}, t_n, T_n)$

the distance $d(x)$ and the predictive uncertainty σ . Formally, the DAC is given by:

$$\text{DAC} = \frac{\sum_{i=1}^N (d_i - \bar{d})(\sigma_i - \bar{\sigma})}{\sqrt{\sum_{i=1}^N (d_i - \bar{d})^2} \sqrt{\sum_{i=1}^N (\sigma_i - \bar{\sigma})^2}}, \quad (38)$$

where d_i is the distance of the i -th test sample to the training dataset, σ_i is its associated predictive uncertainty, and \bar{d} , $\bar{\sigma}$ are their respective sample means. Ideally, test points that are farther from the training dataset should exhibit higher predictive uncertainty, and vice versa. A higher DAC value indicates superior performance of the uncertainty quantification mechanism in capturing input-dependent reliability.

B.4 Training Strategy of PCNN

Algorithm 2 outlines the custom training step of the PCNN. At each training step, the model processes two complementary input streams: (1) the TFR representation, $\mathcal{X}_{\text{batch}\sim\text{TFR}}$, and (2) structured inputs that encode physical parameters, $\mathcal{X}_{\text{batch}\sim\text{phys}}$ (see Table 7 for physical variables). The model first computes the prediction for the data-driven stream (\hat{y}) and then compares the predictions to the ground truth labels (y) to compute loss using Eqn. 10 (for PC-SNGP) or Eqn. 16 (for PC-SNER). Moreover, the Physics-constrained pathway introduces domain knowledge by evaluating how well the model’s behavior aligns with known physical laws. This is done by using automatic differentiation to compute the gradient ($\frac{\partial D}{\partial t}$) of the physical prediction D_{pred} with respect to (t) , which is then compared to the expected output (D'_{phys}) from the theoretical model (D_{coupled}) from Eqn. 21. A composite loss $\mathcal{L}_{\text{total}}$ function combines both the $\mathcal{L}_{\text{data}}$ and $\mathcal{L}_{\text{phys}}$, weighted by parameters derived in Eqn. 2, balancing empirical accuracy and physical consistency. During backpropagation, gradients from both loss components guide parameter updates, enabling a multi-objective optimization process. This dual-stream architecture helps ensure that the learned representations capture patterns in the data and follow the core principles of the underlying physical system.

Algorithm 2 Training step of the PCNNs

Require: Input batch: $\mathcal{X}_{\text{batch}}, y_{\text{true}}$, Physics inputs: Load, RPM, $t_{\text{batch}}, T_{\text{batch}}$, Model \mathcal{M}_{θ} with parameters θ , Adam optimizer \mathcal{O} , Physical model k_{phys} , \mathcal{L}_{MLE} , \mathcal{L}_{ER}

- 1: Data prediction: $\hat{y} \leftarrow \mathcal{M}_{\theta}(X_{\text{batch}})$
- 2: Calculate data loss: $\mathcal{L}_{\text{data}} \leftarrow \mathcal{L}_{\text{MLE}} \parallel \mathcal{L}_{\text{ER}}(y, \hat{y})$
- 3: Physical input: $\mathcal{X}_{\text{phys}} \leftarrow \text{concat}(\mathbf{0}_{N \times 14}, t_{\text{batch}}, T_{\text{batch}})$
- 4: Enable gradient tracking for $\mathcal{X}_{\text{phys}}$
- 5: Physical prediction: $D_{\text{pred}} \leftarrow \mathcal{M}_{\theta}(X_{\text{physics}})$
- 6: Automatic differentiation: $\frac{\partial D}{\partial t} \leftarrow \nabla_{X_{\text{phys}}} D_{\text{pred}}[:, 14]$
- 7: Physical output: $D'_{\text{phys}} \leftarrow D_{\text{coupled}}(t_{\text{batch}}, \text{Load}, \text{RPM}, T_{\text{batch}})$
- 8: Physical loss: $\mathcal{L}_{\text{phys}} \leftarrow \mathcal{L}_{\text{MLE}} \parallel \mathcal{L}_{\text{ER}}\left(\frac{\partial D}{\partial t}, D'_{\text{phys}}\right)$
- 9: Total loss: $\mathcal{L}_{\text{total}} \leftarrow w_1 \mathcal{L}_{\text{data}} + w_2 \mathcal{L}_{\text{phys}}$
- 10: Compute gradients: $\nabla_{\theta} \mathcal{L}_{\text{total}}$
- 11: Update parameters: $\theta \leftarrow \mathcal{O}(\theta, \nabla_{\theta} \mathcal{L}_{\text{total}})$
- 12: **return** $\mathcal{L}_{\text{total}}, \mathcal{L}_{\text{data}}, \mathcal{L}_{\text{phys}}$

Table 7: Physical parameters and values dataset

| Physical variable | PRONOSTIA | XJTU-SY |
|--|-----------------------------|-----------------------------|
| C (Dynamic load rating) | 4000 N | 12000 N |
| p (Fatigue law exponent) | 3.0 | 3.0 |
| q (EDV load exponent) | 4.0 | 4.0 |
| β (Fatigue-EDV coupling coefficient) | 1×10^{-6} | 1×10^{-6} |
| ϕ (EDV growth coefficient) | 1×10^{-5} | 1×10^{-5} |
| D_m (Ball diameter) | 0.025 m | 0.035 m |
| k_B (Boltzmann constant) | 8.617×10^{-5} eV/K | 8.617×10^{-5} eV/K |
| E_a (Activation energy) | 0.1 eV | 0.1 eV |
| E_{vis} (Viscosity activation energy) | 0.1 eV | 0.1 eV |
| T_0 (Reference temperature) | 298 K | 298 K |
| T_a (Ambient temperature) | 298 K | 298 K |
| α (Viscosity degradation coefficient) | 1×10^{-5} | 1×10^{-5} |
| ν_0 (Baseline lubricant viscosity) | 1×10^{-5} | 1×10^{-5} |
| k_o (Oxidation rate coefficient) | 1×10^{-4} | 1×10^{-4} |
| O_{max} (Maximum oxidation level) | 1.0 | 1.0 |
| A_v (Archard wear coefficient) | 1×10^{-5} | 1×10^{-6} |
| A_a (Roughness-induced wear coefficient) | 1×10^{-6} | 1×10^{-6} |
| H_{hard} (Material hardness) | 1.5×10^9 Pa | 1.5×10^9 Pa |
| γ_r (Roughness evolution from wear) | 1×10^{-3} | 1×10^{-3} |
| δ_c (Roughness evolution from debris) | 1×10^{-5} | 1×10^{-5} |
| ρ (Debris generation coefficient) | 1×10^6 | 1×10^6 |
| η (Volume saturation coefficient) | 1×10^6 | 1×10^6 |
| ζ (Roughness saturation coefficient) | 1×10^{12} | 1×10^{12} |
| γ_w (Wear contribution weight) | 0.5 | 0.1 |
| ζ_L (Thermal contribution weight) | 0.5 | 0.1 |
| mc_p (Mass times specific heat) | 3.77×10^6 | 3.77×10^6 |
| μ_f (Friction coefficient) | 0.005 | 0.005 |
| h_A (Heat transfer coefficient) | 5.0 | 5.0 |
| ξ (Oxidation exothermic contribution) | 100.0 | 100.0 |